2009

# SiO2 nanosphere textured back reflectors for enhanced light trapping in amorphous and nanocrystalline silicon solar cells

Ryan Boesch
*Iowa State University*

## Recommended Citation

Boesch, Ryan, "SiO2 nanosphere textured back reflectors for enhanced light trapping in amorphous and nanocrystalline silicon solar cells" (2009). *Graduate Theses and Dissertations*. 10508.
https://lib.dr.iastate.edu/etd/10508

# $SiO_2$ nanosphere textured back reflectors for enhanced light trapping in amorphous and nanocrystalline silicon solar cells

by

Ryan Paul Boesch

A thesis submitted to the graduate faculty
in partial fulfillment of the requirements for the degree of
MASTER OF SCIENCE

Major: Electrical Engineering

Program of Study Committee:
Vikram Dalal, Major Professor
Rana Biswas
Kristen Constant

Iowa State University
Ames, Iowa
2009

# DEDICATION

I dedicate this thesis to the memory of my father. You were my role model and the inspiration that made me the person I am today.

# TABLE OF CONTENTS

# LIST OF FIGURES

# LIST OF TABLES

# ABSTRACT

Silica microspheres were investigated as a back surface texturing agent for hydrogenated amorphous (a-Si:H) and nanocrystalline (nc-Si:H) silicon solar cells. Absorption of long wavelength photons (>600nm) is minimal for a-Si:H and nc-Si:H thin films which limits the efficiency of thin-film solar cells. Textured back reflectors are often used to increase the efficiency of these solar cells by diffusely reflecting light and trapping it in the absorbing layer.

In this research, stainless steel substrates were spin coated with silica spheres to add texture. After a post-anneal, silver was deposited on the substrates. Two sphere diameters (250nm and 500nm) were investigated for their impact on diffuse reflection versus wavelength. It was found that the peak in diffuse reflection could be controlled by varying the sphere diameter. The thickness of the silver layer was determined by maximizing the total reflection, and diminishing returns were found for a silver layer greater than 300nm.

External quantum efficiency measurements were used to characterize carrier collection versus wavelength. An increase in carrier collection at long wavelengths (>600nm) was observed for both a-Si:H and nc-Si:H solar cells on the silica sphere textured substrates. The thin a-Si:H solar cells often shorted out during testing which limits the industrial application of this back reflector. Shorting was not found to be a problem with the nc-Si:H devices.

# CHAPTER 1. INTRODUCTION

## 1.1 Background

Due to environmental concerns and diminishing supplies of fossil fuels, renewable energies will become an increasingly significant portion of the total global energy production in the near future. All renewable energy sources depend on the energy from the electromagnetic radiation from the sun except tidal energy and geothermal energy which use gravitational energy from the moon and the heat from the core of the earth, respectively. Of the solar renewable energy sources, solar cells most directly convert solar radiation into useable energy, converting photons directly into electric current.

Before solar cells can become a major source of energy it is critical they can be manufactured economically with costs per unit energy on the order of coal and nuclear power plants(1). Crystalline silicon (c-Si) solar cells have enjoyed a majority share of the photovoltaic industry but have reached cost scaling limits due to the high demand for crystalline silicon wafers. An alternative method for making silicon solar cells is to grow hydrogenated amorphous silicon (a-Si:H) or nanocrystalline silicon (nc-Si:H) layers on cheap substrates using chemical vapor deposition (CVD) techniques. This uses significantly less silicon because silicon wafers used for photovoltaics are 200-300μm thick and nc-Si:H/a-Si:H solar cells are on the order of 1μm.

There are two basic cell structures that are used for a-Si:H or nc-Si:H solar cells depending on the deposition sequence: the superstrate (p-i-n) or substrate (n-i-p)(2). These structures are displayed schematically in Figure 1.1. For the n-i-p structure, light passes through a top contact made of a transparent conducting oxide (TCO). The composition of this layer is typically indium tin oxide (ITO) or zinc oxide (ZnO), each compound having a high transparency and conductivity. Light passes through the thin boron doped p-layer and is ideally absorbed in the intrinsic layer generating an electron-hole pair (EHP) that is driven to the n/p layer by the internal electric field. In each structure, the light enters through the p-layer to support hole collection due to the lower mobility of holes as compared to electrons(2). This is necessary because the highest percentage of light is absorbed at the top of the intrinsic layer.

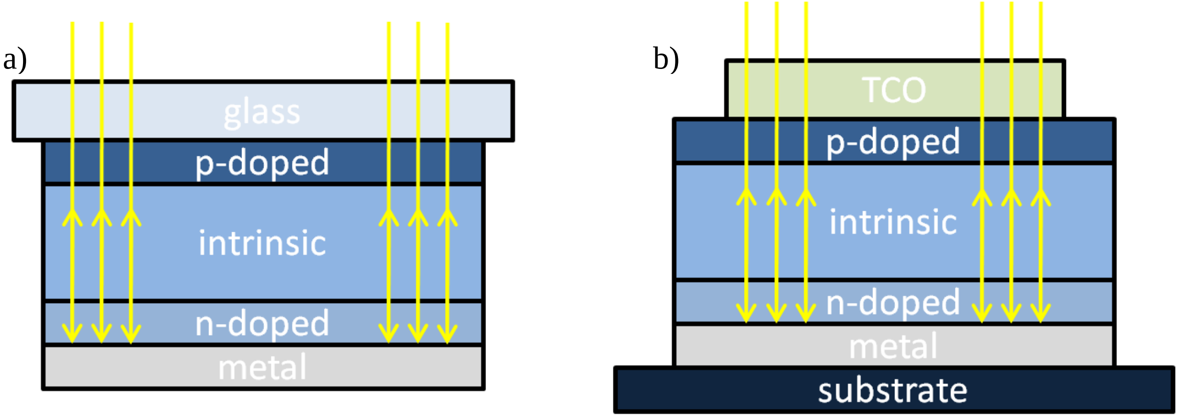

**Figure 1.1 Schematic representations of a) p-i-n superstrate and b) n-i-p substrate with specular back reflectors**

## 1.2 Research Motivation

Many of the long wavelength photons will not be absorbed in the solar cell structures shown in Figure 1.1 because the path length is only two times the thickness of the intrinsic layer. The probability of absorption is given by the equation,

$$P_{abs} = 1 - e^{-2t_i\alpha}$$

where $t_i$ is the thickness of the intrinsic layer and α is the absorption coefficient. Figure 1.2 shows the absorption coefficient versus photon energy for nc-Si:H, c-Si, and a-Si:H.

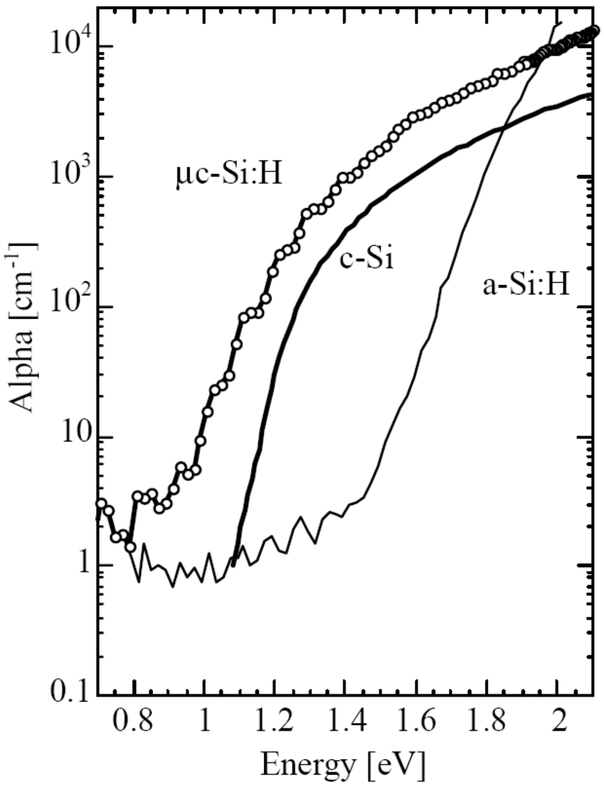

**Figure 1.2 Absorption of µc-Si:H, c-Si, and α-Si:H (1)**

Assuming an intrinsic layer thickness of 0.5µm for both a-Si and nc-Si, Table 1.1 gives the probability of photon absorption at various wavelengths.

**Table 1.1 Probability of photon absorption at various wavelengths**

| Wavelength (nm) | Absorption Probability (nc-Si:H) | Absorption Probability (a-Si:H) |
|---|---|---|
| 600 | 59.3% | 63.2% |
| 650 | 55.1% | 55.1% |
| 700 | 36.2% | 2.9% |
| 750 | 22.1% | 1.0% |
| 800 | 18.1% | 0.2% |
| 850 | 13.5% | 0.03% |
| 900 | 5.8% | 0.01% |

It is clear from the data in Table 1.1 that a large number of longer wavelength photons are not being absorbed. The range from 800nm to 1100nm contains 36.2% of the solar photons with energy above the band gap of nc-Si:H(2). One method to increase absorption is to increase the thickness of the intrinsic layer, but the thickness is limited by the growth processes of a-Si:H and nc-Si:H. Furthermore, the stabilized fill factor decreases with increasing i-layer thickness(3).

To overcome this trade-off, it is necessary to use light trapping schemes(3). A method for collecting long wavelength light is to replace the specular back reflector in Figure 1.1 with a diffuse back reflector. Figure 1.3 demonstrates this effect for the superstrate (p-i-n) and substrate (n-i-p) structures with an arbitrary Lambertian[1] back reflector.

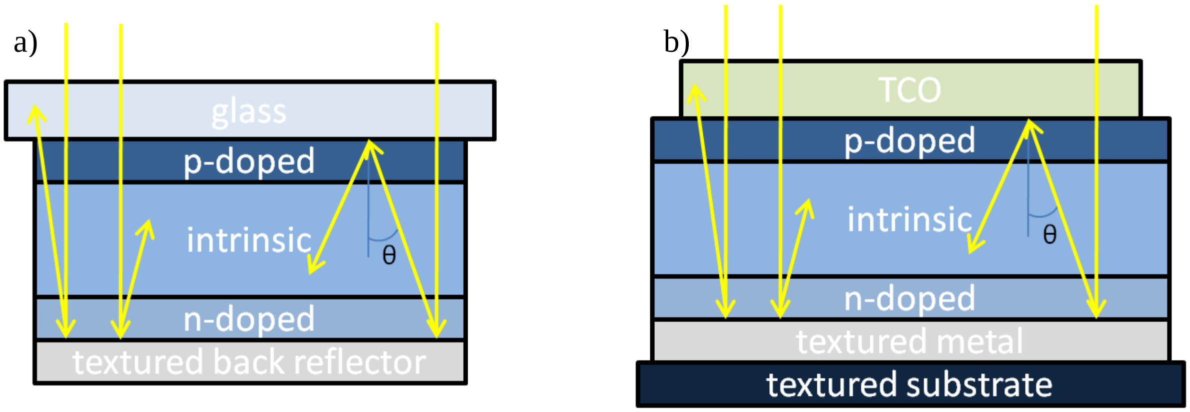

**Figure 1.3 Schematic representations of a) p-i-n superstrate and b) n-i-p substrate demonstrating total internal reflection for an arbitrary Lambertian back reflector**

Light reflected at a reflection angle exceeding the critical angle,

$$\theta_c = \sin^{-1}\left(\frac{n_1}{n_2}\right)$$

will experience total internal reflection. The refractive index of a-Si:H is given by the equation(4),

$$n_{a-Si} = \frac{3.028x10^5}{\lambda^2} + 2.595$$

---

[1] A Lambertian surface is isotropic in that it reflects light of all wavelengths uniformly in all directions.

where λ is the wavelength of light in nanometers. The total internal reflection angle can then be calculated at each wavelength. It should be noted that as the wavelength increases, the total internal reflection angle also increases. This implies that it is more difficult to trap long wavelength light. For light with a wavelength of 800nm, the critical angle is $19^o$. The refractive index of nc-Si formed by PECVD was found to be 1.71(5) which gives a critical angle of $35.8^o$ at the air/nc-Si interface.

For a Lambertian back reflector, statistical optics can be used to show that the maximum path length increase is $4n^2$ where n is the refractive index of a-Si:H or nc-Si:H(6). This corresponds to a path length increase by a factor of about 28 for a-Si at 800nm and about 11.7 for nc-Si. This assumes 100% reflection from the back reflector which is not realizable in practice. In reality, the maximum obtainable enhancement factor is closer to 10(7).

Traditional crystalline silicon surface texturing is on an order larger than the thickness of nc-Si and a-Si thin film solar cells. It is necessary that textures have features on the same order of magnitude or less than the thickness of the film so that device shorting and device degradation is minimized(8). In this research, a new texturing technique is proposed and fabricated that meets this criterion. Figure 1.4 shows a schematic diagram of the proposed back reflector and solar cell structure. Silica micro-spheres (0.25µm and 0.5µm) texture the stainless steel substrate and are coated with a layer of highly reflecting silver.

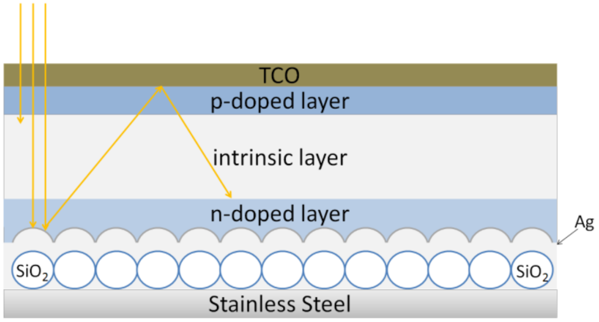

**Figure 1.4 Schematic representation of the proposed p-i-n solar cell structure with a silica sphere textured back reflector**

## 1.3 Literary Review

In this section a discussion is given on current solar cell light trapping techniques. Also, a review of previous methods of microsphere monolayer deposition is made.

### 1.3.1 Solar Cell Light Trapping

Many light scattering techniques have been reported in the literature. The desired properties for a good substrate include high reflection, high light scattering, surface roughness features on the order of the thin film thickness, and low resistivity. A good superstrate should have the same properties but should have high transmission instead of reflection. Asahi Glass Co. has developed $SnO_2$ coated glass substrates on which the solar cells with the maximum efficiencies have been built(3). Unfortunately, these substrates are expensive and not scalable to large area industrial solar cells(3). In this section a review of current scalable light trapping techniques is made.

#### 1.3.1.1 Etched ZnO/Glass Superstrate

A popular light scattering technique is to sputter ZnO:Al on a glass substrate and then texture etch the surface with dilute HCl(3)(9)(10). This technique is of particular interest because most a-Si and nc-Si solar cell manufacturers already have sputtering systems in place(3). Also, sputtering is a low temperature process that is compatible with preceding process steps(3). Figure 1.5 shows SEM images of a ZnO film before and after etching in diluted HCl. The ZnO films can be deposited by either d.c. or r.f. sputtering. Films formed with d.c. sputtering exhibit increased resistance to etching. Also, deposition temperature and pressure influence the etching resistance of both r.f. and d.c. sputtered films(9). Typical pressures for d.c. ZnO sputtering are in the range of 5-10 mTorr and for r.f. sputtering the range is 1-5 mTorr(10).

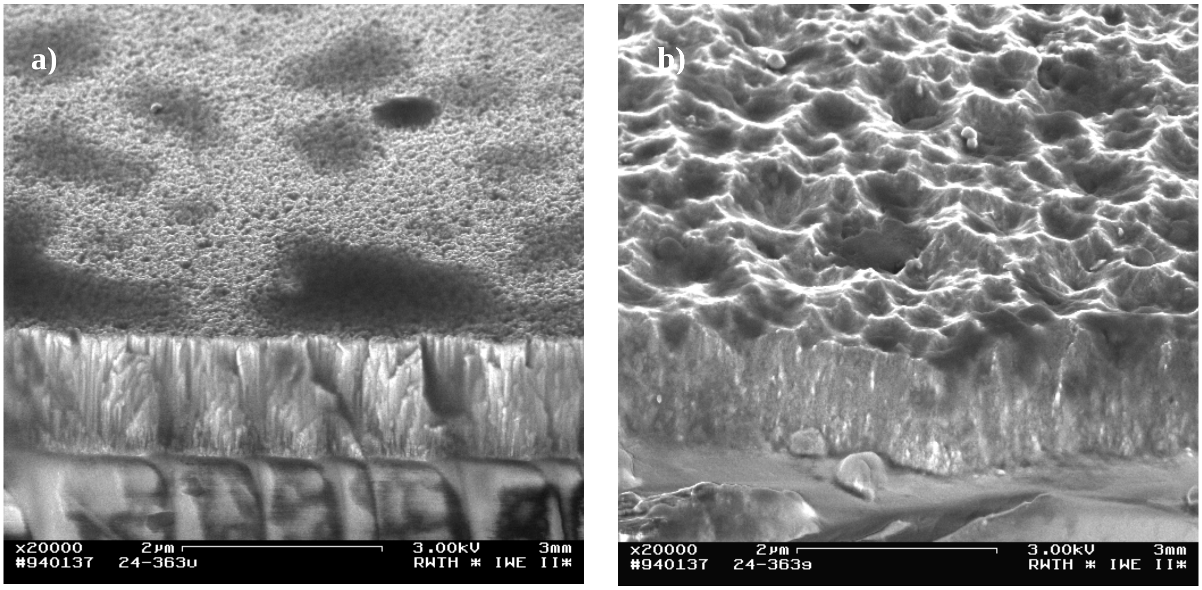

**Figure 1.5. SEM images of ZnO film a) before and b) after dipping in dilutted HCl (3)**

Superstrate a-Si p-i-n solar cells grown on the glass/texture ZnO substrates have shown significant increases in quantum efficiency. Figure 1.6 shows the quantum efficiency of an a-Si solar cell prepared on smooth ZnO and textured ZnO. The increases in QE are most significant in the regions beyond 600nm, which is expected because photons with lower wavelengths are trapped on the first pass through the intrinsic layer.

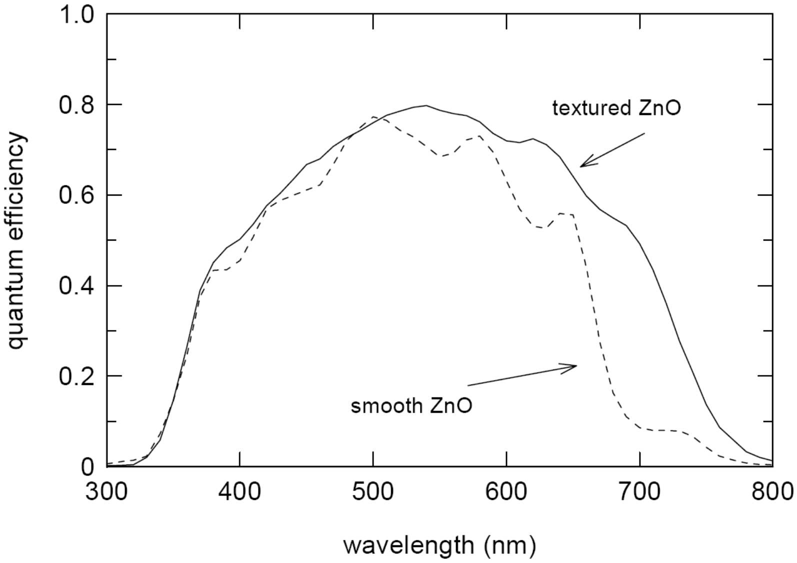

**Figure 1.6 Quantum efficiency of two a-Si:H p-i-n solar cells prepared on smooth and textured ZnO (9)**

Using this substrate stacked junction a-Si/a-Si cells showed efficiencies of 10.2% demonstrating an increase in efficiency when compared to reference cells prepared on Asahi U type substrates with efficiencies of 9%(9).

### 1.3.1.2 Etched ZnO/Ag Back Reflector

Another light scattering technique again makes use of the texture etching property of ZnO, but it is used in an n-i-p substrate cell structure. ZnO is sputtered on a substrate and then etched in diluted HCl to add texture as shown in Figure 1.5. Silver is then evaporated or sputtered on ZnO film producing a back reflector with high reflexivity and scattering.

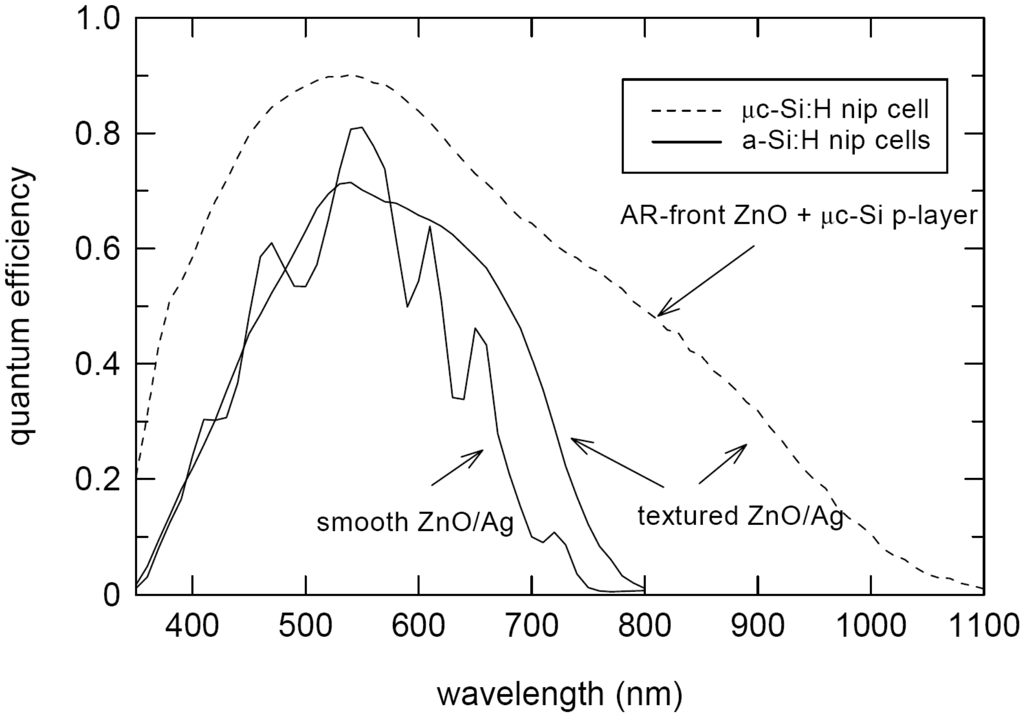

**Figure 1.7. Quantum efficiency of two a-Si:H n-i-p solar cells codeposited on smooth and texture-etched ZnO/Ag coated glass substrates and the quantum efficiency of a μc-Si solar cell prepared on texture-etched ZnO/Ag**

Figure 1.7 shows the quantum efficiency of an a-Si:H n-i-p solar cell prepared on a textured ZnO/Ag substrate as well as a reference solar cell prepared simultaneously on a smooth ZnO/Ag substrate. Once again, the increases in quantum efficiency are mostly notable for wavelengths greater than 600nm. Also shown in Figure 1.7 is the QE of a nc-Si solar cell that extends out to 1100nm due to the lower band gap of µc-Si.

The back reflector in this research textures the substrate at room temperatures and atmospheric pressure with no dangerous chemicals. This is a significant advantage over textured ZnO back reflectors which require expensive sputtering and an etch with HCl.

### 1.3.1.3 Sol-gel Silica Sphere Dip-Coating

Pacific Solar developed a technique termed Crystalline Silicon on Glass (CSG) to create 2µm thin crystalline silicon solar cells with a conversion efficiency of 8.2%(11). A schematic view of the CSG structure is given in Figure 1.8 a). The substrate is glass textured by coating with silica nanospheres. A 1.6µm layer of silicon is deposited using silane gas chemical vapor deposition (CVD) and is then heat treated to crystallize the layer. Due to the nature of CVD, the silicon layer conforms to the roughness of the surface. A thin layer of aluminum is deposited on the top of the crystallized silicon which exhibits the same roughness of the substrate and acts as a back reflector. As demonstrated in Figure 1.8 a), a photon passes in through the glass substrate and reflects off the aluminum back surface. It will then reflect back from the glass/c-Si interface if the angle of incidence is sufficient.

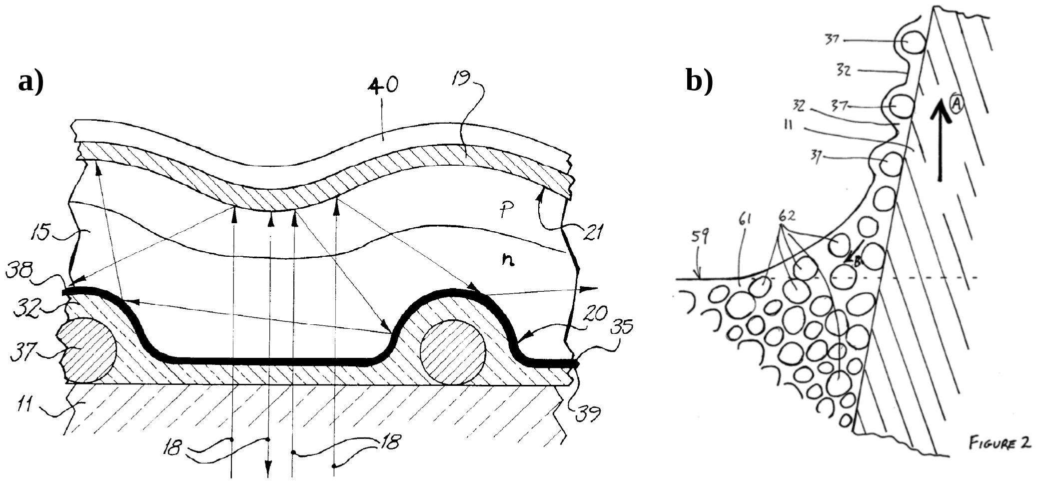

**Figure 1.8 a) Schematic view of the CSG solar cell structure and b) silica sphere sol-gel dip coating process (8)**

The substrate is prepared using a patented technique in which a glass substrate is lowered into a sol-gel glass solution with suspended silica ($SiO_2$) beads. As the substrate is pulled from the solution, a thin layer of glass sol-gel and silica beads remain. This process is represented in Figure 1.8 b).The thickness of the sol-gel layer and the surface density of the silica spheres can be accurately controlled by the pull rate of the substrate and the viscosity of the sol-gel (12).

### 1.3.2 Sphere Deposition Techniques

Many methods for forming nano/microsphere monolayers have been reported in the literature. In this section, the two methods that were applied most frequently in this research are reviewed.

#### 1.3.2.1 Langmuir-Blodgett (LB) Technique

One commonly used method to form microsphere or nanosphere monolayers is the Langmuir-Blodgett method. In this method, a monolayer of particles self assembles at the air/water or air/oil interface. This monolayer can then be transferred to a substrate by slowly pulling a substrate through the monolayer.

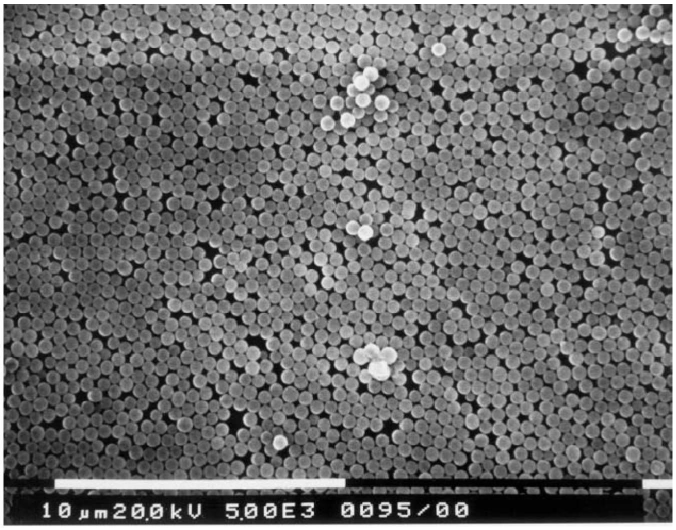

**Figure 1.9. SEM image of a monolayer of 450nm spheres deposited on glass microscope slides by the Langmuir-Blodgett technique(13)**

Silica sphere monolayers have been formed by the Langmuir-Blodgett method by controlling the hydrophobic-hydrophilic properties of the particles which were dissolved in ethanol(13). The solution was ultrasonicated for 30 minutes and then dropped into water. After the monolayer self assembled at the air/water interface, a glass microscope slide was pulled vertically at 1 mm/mi (13). Figure 1.9 shows an SEM image of a monolayer of 450nm spheres formed with this technique.

This technique was explored for this research but eventually abandoned for a more simplistic spin coating technique.

### 1.3.2.2 Microsphere Spin Coating

J. Hulteen et al. developed a method for depositing nanospheres on an arbitrary substrate for nanoscale lithography(14). Polystyrene nanospheres with a diameter of 264nm±7nm were purchased in a water solution from Interfacial Dynamics Corporation. This solution was then diluted in the surfactant Triton X-100/methanol 1:400 by volume(14). The solution was spun onto the substrate at 3600RPM and with a 90% success rate in which large defect free packed sphere regions were observed over the entire substrate.

### 1.3.2.3 Bragg Diffraction of Nanospheres

P. Jiang et al. developed a method to form a non-closed packed monolayer of 315nm silica spheres on a wafer by spin-coating. The wafer was primed with APTCS and was spin coated at 200RPM for 120s, then at 300RPM for 120s, then at 1000RPM for 60s, followed by 3000RPM for 20s, 6000RPM for 20s, and finally 8000RPM for 360s(15). Figure 1.10 a) shows a cross-sectional SEM image of a monolayer made by this process. The reflectivity spectrum for a sample with a lattice spacing of $\sqrt{2}D$ was calculated using a scalar wave approximation (SWA) and is shown as the red curve in Figure 1.10 b). The measured response for a fabricated monolayer with approximate $\sqrt{2}D$ spacing is shown as the black curve in Figure 1.10 b)(15). A minimum in reflection occurs at a wavelength slightly greater than the sphere diameter of 315nm, and a peak occurs at a wavelength slightly greater than two times the sphere diameter. This is due to the Bragg diffraction constructive and destructive interferences. These maxima and minima have been observed in the reflection spectrum of the back reflectors in this research.

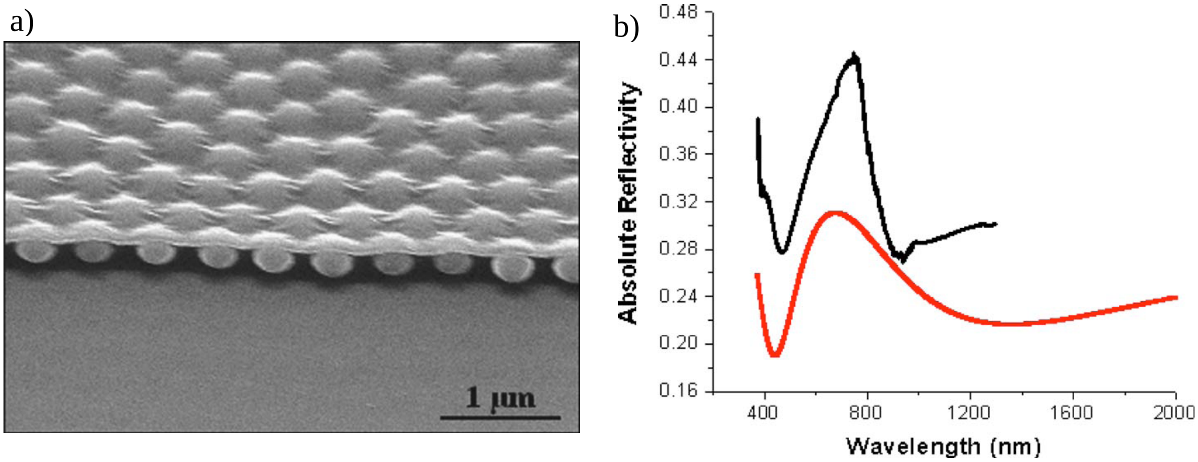

**Figure 1.10. a) Cross-sectional SEM image of a monolayer made by spin coating and b) spectral reflectivity of the monolayer in black and theoretical reflectivity in red(15)**

# CHAPTER 2. METHODOLOGY AND PROCEDURES

## 2.1 Nanosphere Deposition

Silica ($SiO_2$) microspheres were purchased from Fiber Optic Center, Inc. The spheres (called AngstromSphere) were 0.25µm and 0.5µm with a standard deviation of less than 10%. Figure 2.1 shows an SEM image of the silica spheres. Table 2.1 summarizes the physical properties of the spheres.

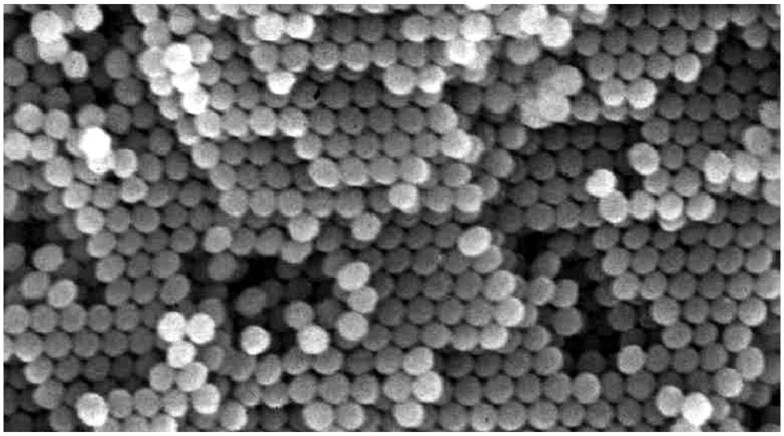

**Figure 2.1. SEM photograph of AngstromSphere uniform silica spheres(16)**

**Table 2.1. Summary of the physical properties of AngstromSphere silica spheres (16)**

| | |
|---|---|
| Size | 0.25µm and 0.5µm |
| Density | 2.0 grams/cc |
| Structure | Amorphous |
| Purity | >99.9% |
| Dielectric Constant | < 3.8 |
| Refractive Index | ~1.38 – 1.46 |

The first step in the silica sphere deposition process is to prepare the colloid. The AngstromSphere silica spheres came in a dry form. The surface of the silica spheres in this form has a large quantity of hydrophilic silanol (Si-OH) groups and therefore the spheres disperse well in water. Triton X-100 was used as a surfactant to lower the surface tension of the suspension and allow easier spreading of the spheres during spin coating. To determine the amount of surfactant that was necessary, a sweep of concentrations was performed. A solution was prepared with 92% Ethanol and 8% silica spheres by weight and ultrasonicated for 1 hour after the addition of Triton X-100. Three substrates were then spin coated at 500RPM for 60 seconds and are shown in Figure 2.2. Substrate S59 was spin coated with no Triton X-100, and it is visibly clear that the spheres were not able to spread evenly across the substrate. Alternatively, S61 was spin coated with 5.9% Triton X-100 (by weight) and no spheres attached to the stainless steel surface. S60 was spin coated with 0.89% Triton X-100 and a sphere monolayer was formed.

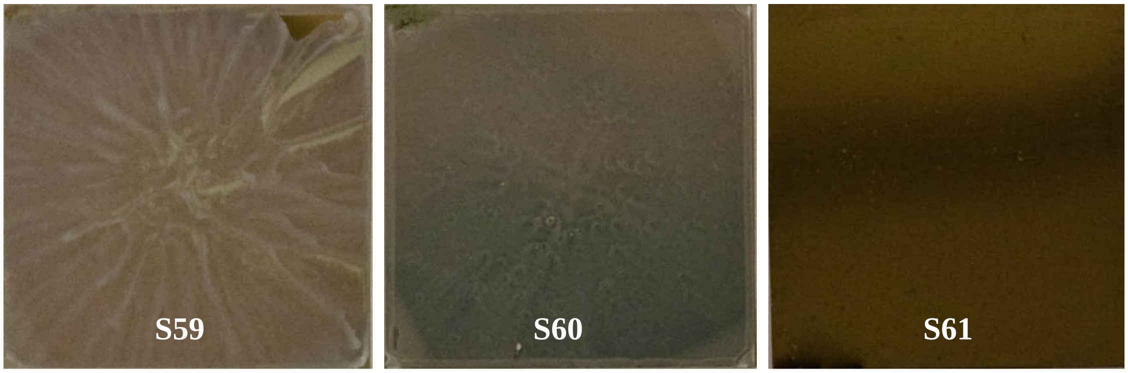

**Figure 2.2. Substrates S59, S60, and S61 formed by spin coating colloids with 0%, 0.89%, and 5.7% of Triton X-100 by weight**

Spin coating water/Triton-X100/silica sphere colloids resulted in large clusters of agglomerated silica spheres. It was found that adding ethanol to the colloid reduced this effect, but purely ethanol colloids also resulted in large clusters of agglomerated spheres. Figure 2.3 shows SEM images of silica sphere agglomeration for three stainless steel substrates spin coated at 500 RPM. The colloids used were 7% silica sphere, 1% Triton X-100, various amounts of ethanol, and the remaining percentage DI water. Each colloid was ultrasonicated for 1 hour.

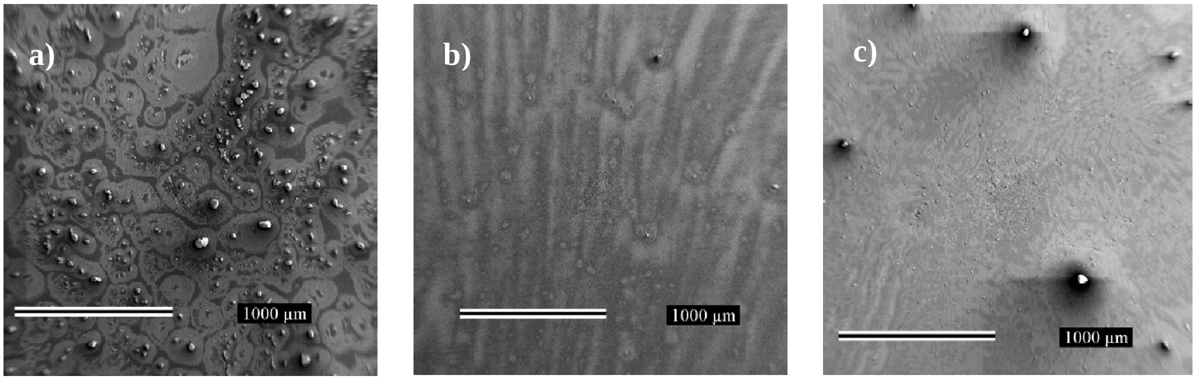

**Figure 2.3. SEM images of silica sphere agglomeration for spin coated substrates using colloids of 7% silica spheres (by weight) a) 0% ethanol b) 30.5% ethanol and c) 93% ethanol**

After these experiments, the optimum solution was determined to be 0.5% Triton X-100, 7% silica spheres, 25% ethanol, and 67.5% deionized water (DI) water. This solution is summarized in a chart in Figure 2.4 and was used for all colloid depositions in this research.

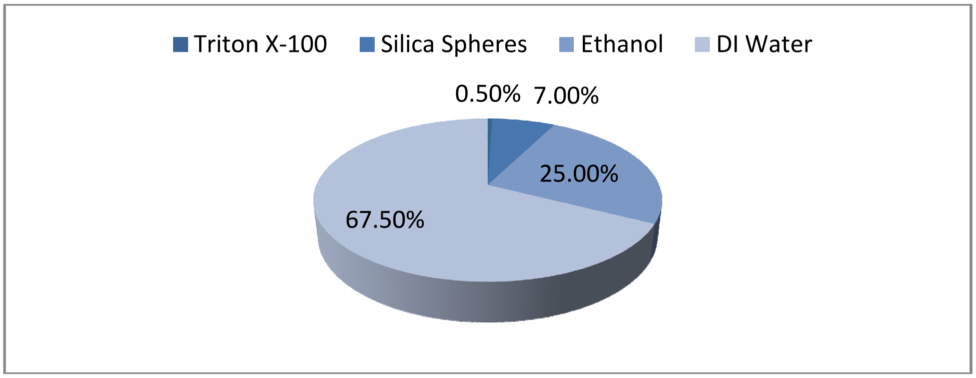

**Figure 2.4. Summary of the colloid composition**

After the colloid is formed it is dispersed by ultrasonication for one hour. The stainless steel substrates are cleaned before spin coating in three steps: a 15 minute acetone boil, a 15 minute methanol ultrasonication, and a 15 minute boil in a solution of equal parts DI water, ammonium hydroxide, and hydrogen peroxide. Five to ten drops of the colloid are then dropped at the center of a cleaned stain steel (SS) substrate resting on a spin coater. The spin coater can be controlled to spin at a rate between 400RPM and 10000RPM. The spin rate was not fixed but instead left as a design variable for the substrates.

The next step in the sphere deposition process is a post-anneal. The anneal was performed at 500$^{o}$C for 30 minutes. The anneal is necessary because a small amount of residual moisture from the colloid remains on the substrate after the sphere coating process. A solar cell was made on a substrate without a post-anneal and all deposited contacts were shorted. Figure 2.5 a) shows an SEM image of a defect in the a-Si:H solar cell formed without a substrate anneal. Figure 2.5 b) shows a fissure formed in the a-Si:H thin film that is a clear indicator of evaporation during the film growth.

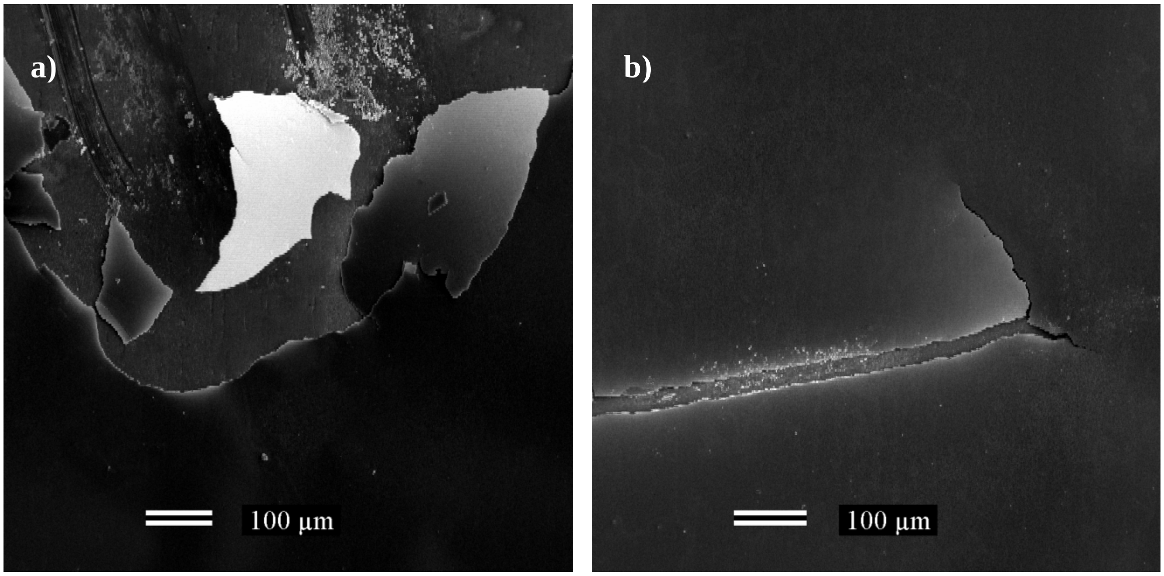

**Figure 2.5. Defects resulting from residual moisture evaporation during the a-Si:H film growth**

Table 2.2 gives a summary of the silica sphere deposition process designed.

**Table 2.2. Summary of silica sphere deposition steps**

| | |
|---|---|
| Step 1 | Prepare a colloid: 0.5% Triton X-100, 7% silica spheres, 25% ethanol |
| Step 2 | Disperse spheres with 1 hour ultrasonication |
| Step 3 | Drop 5 to 10 drops to center of cleaned SS substrate |
| Step 4 | Spin at a rate from 400RPM to 10000RPM |
| Step 5 | Anneal at 500$^{o}$C for 30 minutes |

After the anneal, the silica spheres are attached strongly to the stainless steel substrate and are not removed with high pressure $N_2$ gas. The next step is to evaporate silver on the substrate.

## 2.2 Evaporation

The first step of the evaporation process is to bring the evaporation chamber to a vacuum. This decreases the evaporation temperature of the metal and ensures that the metal vapor has a clear path to the substrate. A roughing pump is used to reduce the pressure to just less than 1 Torr and a vertical turbo pump then brings the chamber down to the desired vacuum pressure of ~ 1 μTorr. Depending on the state of the evaporation chamber, a varying number of $N_2$ purges are necessary to bring the chamber to the desired vacuum.

With the chamber at vacuum, the metal evaporation process can begin. For silver evaporation, a degas step is necessary for the optimum film quality. With the shutter closed, current is increased through the tungsten boat to heat up the silver wire or pellets. The temperature is maintained just below the evaporation point of silver for a period of time. During this time, all compounds on the surface of the silver with an evaporation point less than silver will be “degassed.” During this process the pressure of the chamber will increase. When the pressure returns to the initial value, the current is increased and the evaporation of silver begins.

A Maxtek TM200R thickness monitor is used to simultaneously measure the thickness and growth rate of the film. This is done with a quartz oscillator which changes its resonant frequency due to the mass of material deposited(17). For silver depositions, the growth rate was controlled to be between 0.4 nm to 0.5 nm per second. This rate was determined by previous experiments in our group to form a silver layer with maximum reflectivity. For aluminum evaporations, the vapor needs to have minimum exposure to oxygen and therefore was controlled to be between 3nm and 4nm per second.

## 2.3 PECVD of a-Si:H and nc-Si:H

Chemical vapor deposition (CVD) is a chemical process that is often used to deposit high-purity and accurately controlled thin films. Plasma enhanced CVD (PECVD) is a modification to CVD in which a plasma is used to dissociate precursor gases. In this research, PECVD was used to form a-Si:H and nc-Si:H layers. Diborane and phosphine were introduced to form p+ and n+ layers. Figure 2.6 shows a schematic diagram of the plasma reactor used to deposit all n+, p+, and intrinsic amorphous silicon layers. The chamber is brought up to atmospheric pressure with $N_2$ gas to load the substrate. Due to the horizontal chamber design, the substrate is loaded from the top and is positioned vertical to the ground. This orientation prevents debris from resting on the substrate, falling into the vacuum system, or resting on the electrode.

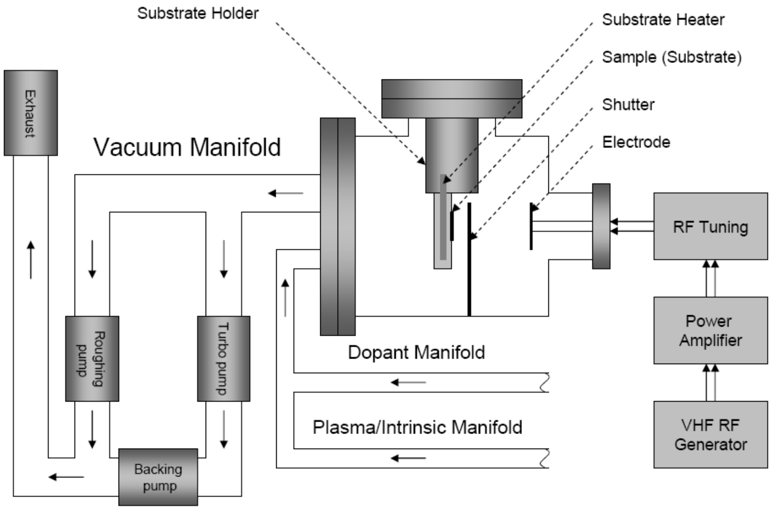

**Figure 2.6. Schematic diagram of the plasma reactor(18)**

With the substrate loaded in the chamber a mechanical roughing pump is used to bring the chamber down to a pressure of about 1 Torr. A horizontal turbo pump then brings the pressure of the chamber down to ~0.1 µTorr. Gas is then introduced into the chamber through different flow lines. It can be seen in Figure 2.6 that the dopant line is kept separate from the intrinsic/plasma line. This is because dopants are parasitic to the intrinsic films.

Intrinsic nc-Si films are deposited in a separate reactor because their performance is particularly limited by parasitic dopants. The plasma line carries hydrogen and helium. The intrinsic line carries silane ($SiH_4$) gas and merges with the plasma line before the reactor. The dopant line carries methane ($CH_4$), phosphine ($PH_3$), and diborane ($B_2H_6$) depending on the desired composition of the film. Methane is used in conjunction with phosphine and silane to form an n+ silicon carbide layer. A normal n+ is formed with just phosphine and silane while a p+ is formed with diborane and silane. The intrinsic layer is formed with just silane.

For all the thin film layers, the gas flow is accurately regulated and the pressure of the chamber is maintained to be on the order of mTorrs by adjusting the turbo pump valve. The substrate is heated and an r.f. power is applied to the electrode. This forms a glow-discharge plasma in which the gases lose electrons which are subsequently accelerated to high energies by the r.f. power. These high energy electrons bombard and dissociate the silane, diborane, and phosphine gases. Using the plasma to dissociate the gases allows the substrate to be at a lower temperature which promotes the growth of amorphous silicon.

Figure 2.7 shows a schematic representation of the a-Si:H solar cell fabricated in this research. The dimensions are indicated correctly but the image itself is not to scale. Similarly, Figure 2.8 shows a schematic representation of the nc-Si:H solar cell fabricated in this project. The total thickness of the amorphous cell is about 510nm which is only two times the size of the 250nm spheres and is similar to the size of the 500nm spheres.

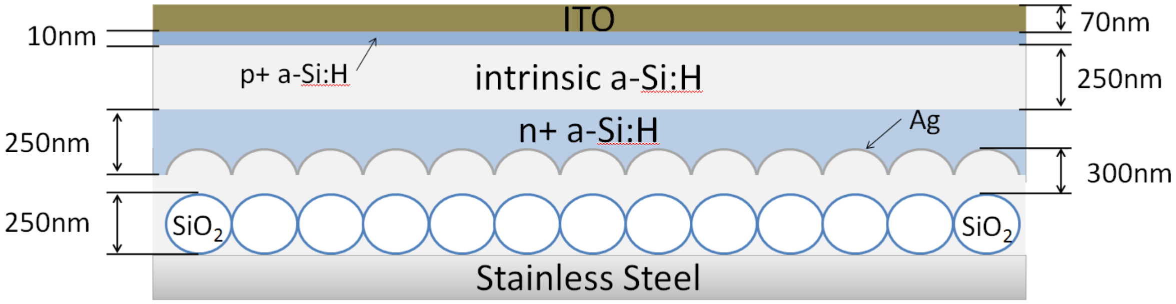

**Figure 2.7. Schematic diagram of the dimensions of the amorphous silicon solar cell fabricated in this project**

This caused trouble during device characterization where device shorting occurred frequently. The thickness of the nc-Si:H device is about 1.8µm which is more than seven times the diameter of the 250nm spheres on which the devices were built. For this reason, device shorting during characterization was not a problem for the nanocrystalline solar cells.

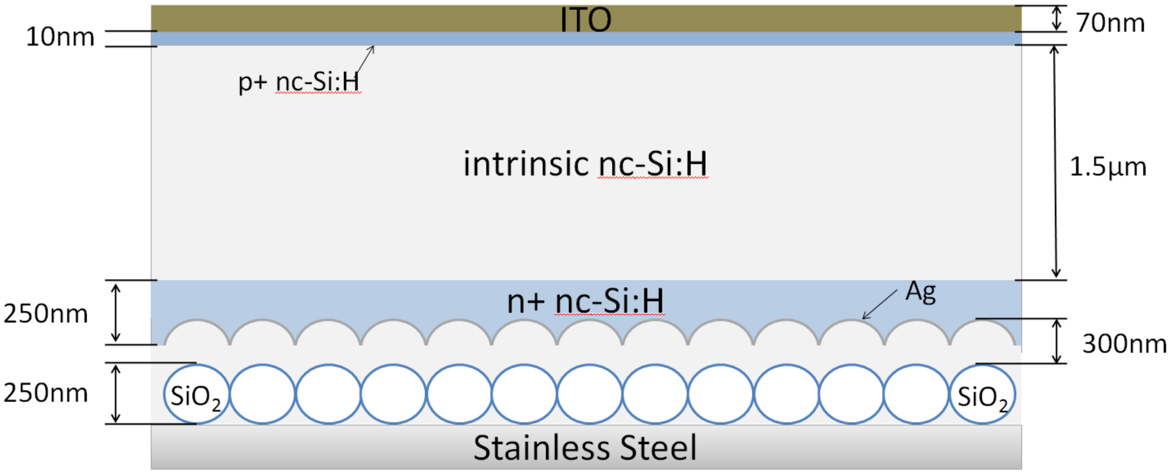

**Figure 2.8. Schematic diagram of the dimensions of the nanocrystalline silicon solar cell fabricated in this project**

## 2.4 ITO Sputtering

A top contact has to be deposited on the solar cell that is both transparent (to allow the passage of light) and conductive (to collect the current). For the solar cells fabricated in this project a 70nm ITO layer is used to form an antireflective top contact(19). The equation that governs the antireflective property of a thin film is(20),

$$nd = \frac{\lambda}{4}$$

This equation, unfortunately, indicates that it is only possible to have the antireflective property at a one wavelength.

The first step of the sputtering process is to bring the chamber down to a vacuum. A roughing pump is used to bring the chamber below 1 Torr, and a vertical turbo pump is then used to bring the chamber down to a base pressure of ~1µTorr. The substrate is then heated to 225°C. Argon and oxygen/argon gas flows are introduced to the chamber in a 400:1 ratio. The base pressure of the chamber is controlled to be 5mTorr by adjusting the turbo pump valve. A d.c. power of 20W is then applied to the electrode. The target is conditioned with the shutter closed for 2 minutes before a deposition for 2.5 minutes. The film growth rate under these conditions is about 4.5A/s, so this deposition time yields a thickness of about 70nm.

# CHAPTER 3. CHARACTERIZATION

## 3.1 Back Reflector Characterization

### 3.1.1 Scanning Electron Microscope (SEM) Imaging

Nanosphere packing density, agglomeration, and back reflector defects were characterized using a JEOL JSM 6100 scanning electron microscope. The maximum magnification is 300000X and the resolution is 40Å which is sufficient to image the 250nm and 500nm spheres used in this research. The chamber is brought to a vacuum by a mechanical roughing pump and a vertical diffusion pump, and the typical pressure during operation is about 20µTorr.

The nanosphere packing density is an important characteristic of the back reflectors and is defined to be the number of spheres times the area of spheres divided by the area of the containing region.

$$Packing\ Density = \frac{\#_{spheres} \cdot \pi \left(\frac{D_{sphere}}{2}\right)^2}{Area}$$

The packing density was characterized using the contrast between the silica spheres and the substrate in the SEM images in a method presented in the Appendix.

### 3.1.2 Total and Diffuse Reflection

The total and diffuse reflections of the back reflectors were measured using Varian's Cary 5000 UV-Vis-NIR spectrophotometer. The wavelength range is from 175nm to 3300nm which fully covers the absorbable wavelengths in both amorphous and nanocrystalline silicon films. The Cary 5000 is a double beam spectrophotometer. Light from the lamp source is focused and then split into two separate time-interleaved beams. In this way, the full intensity of the light source is available to each light path for a half period and the same photo-detector can be used to measure the light from each path for a half period. The intensity of one half period of the light beam is transmitted through or reflected off a sample and detected by the photo-detector. This is then normalized to the intensity of light of the other half period which is the reference beam that is either 100% transmission of 100% reflection.

To measure diffuse reflection the DRA-2500 integrating sphere was used. Light is reflected off of a sample placed at an entrance port to the sphere. The specular reflection is blocked from the sphere, and the diffusely reflected light is reflected by the Lambertian interior surface of the sphere. The sphere will preserve the power of the light but destroy the spatial information effectively integrating the non-specular reflected light. Total reflection is measured in a similar way, but the specular reflection is not blocked and the integrating sphere sums the total reflected light.

## 3.2 Device Characterization

To characterize both nc-Si and a-Si devices quantum efficiency (QE), QE versus voltage, and I-V measurements were taken.

### 3.2.1 I-V Measurement

The first measurement taken on a solar cell in this research is the I-V measurement. This measurement identifies shorted devices and gives information about the quality of a functioning device. The I-V measurement apparatus shines a 120V and 300W ELH Quartzline lamp bulb perpendicular to the device. The ELH bulb is used to imitate the AMI 1.5G light spectrum. It is important that the bulb have a long lifetime because the variation in the spectral irradiance for different bulbs out of the same case is much greater than the change with the bulb age(21).

A reverse bias voltage is applied to the device and the current is measured. This measurement provides the following characteristic parameters: short circuit current ($I_{SC}$), open circuit voltage ($V_{OC}$), fill factor (FF), and efficiency ($\eta$). $I_{SC}$ is a measurement of the current delivered by the device with zero applied voltage (short circuit). $V_{OC}$ is the voltage required so that the device is delivering zero current (open circuit). $I_{SC}$ and $V_{OC}$ correspond to the maximum current and maximum voltage from the device, respectively, but power delivered is zero in each of these cases. Power delivered from the device is the product of the voltage and current of the device. If $V_m$ and $I_m$ are defined as the voltage and current at which the power delivered from the device is a maximum, then the FF can be defined as,

$$FF = \frac{V_m I_m}{V_{OC} I_{SC}}$$

and the efficiency can then be written as,

$$\eta = \frac{I_{SC} V_{OC} FF}{P_{incident}}$$

where $P_{incident}$ is the total power of the incident photon flux, which is typically given as 100mW/cm$^2$ for the AMI 1.5 light spectrum. Shunt and series resistance can also be calculated from the I-V curve. Shunt resistance is taken as the inverse of the slope of the curve at negative voltages because the current contribution due to the pn-junction is very small for negative voltages. The series resistance is taken as the slope at the open circuit voltage because at this point most of the voltage will drop across the series resistance because the small signal diode resistance is small.

### 3.2.2 External Quantum Efficiency (QE)

External quantum efficiency in solar cells is defined as the number of electrons collected divided by the number of photons incident on the device. A schematic of the apparatus used to measure QE is shown in Figure 3.1. A monochromatic light is chopped at a frequency of about 13.5Hz and focused on the device using two focusing lenses and a mirror. The current is converted to a voltage by a transresistance amplifier and then a lock-in amplifier measures the voltage very accurately. Table 3.1 summarizes the wavelengths and applied biases used to measure various solar cells relevant to this research.

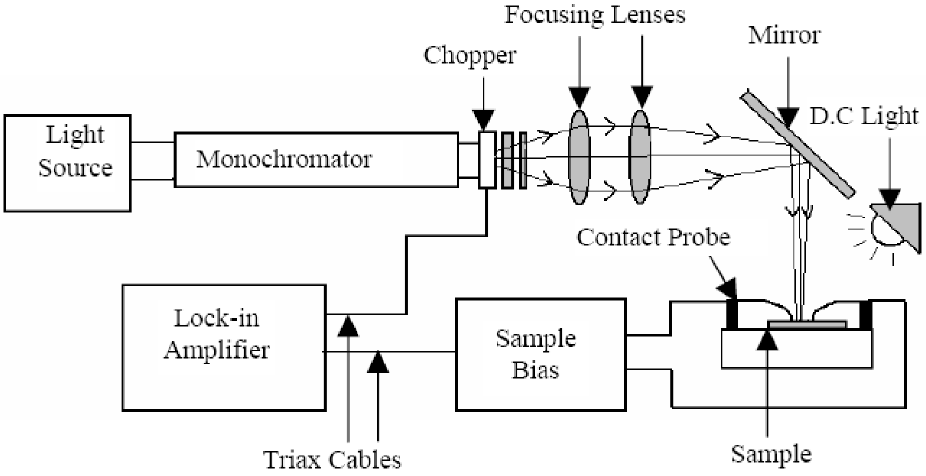

**Figure 3.1. Quantum efficiency measurement apparatus(22)**

The measured voltage is calculated by normalizing it to a reference crystalline silicon cell for which the QE is known.

$$QE_{sample} = QE_{reference}\frac{\left(\frac{V_{sample}}{A_{sample}}\right)}{\left(\frac{V_{reference}}{A_{reference}}\right)}$$

This QE data is then typically normalized with the maximum at 90% so they can be easily compared with other devices.

**Table 3.1. Wavelength range and applied biases for a-Si and nc-Si solar cells with and without back reflectors (BRs)**

| Solar cell type | Wavelength range (nm) | Applied biases |
|---|---|---|
| Amorphous silicon | 400 to 800 | 0V and 0.5V |
| Amorphous silicon with BR | 400 to 800 | 0V and 0.5V |
| Nanocrystalline silicon | 400 to 900 | 0V and -0.5V |
| Nanocrystalline silicon with BR | 400 to 1100 | 0V and -0.5V |

# CHAPTER 4. RESULTS AND DISCUSSION

## 4.1 Diffuse Reflection

### 4.1.1 500nm Silica Sphere Back Reflectors

In this section, diffuse reflection results are given for stainless steel substrates textured with 500nm silica spheres and coated with 150nm of silver. The substrates were prepared with the methodology presented in Chapter 2. A sweep of the spin coating rate from 500RPM to 7000RPM was performed. Silica sphere monolayers were achieved and SEM images of these monolayers can be seen in Figure 4.2 a-f). The silica sphere packing density is a strong function of the spin rate. Figure 4.1 is a plot of the packing density (found using the method in the Appendix) versus the spin rate. The packing density decreased dramatically as the centripetal force during spin coating increased. The dashed line in Figure 4.1 shows the packing density of close packed spheres for reference. Close packed spheres have a packing density of the area of a sphere divided by the area of a unit cell of the sphere, 78.5%.

The diffuse reflection for these substrates is shown in Figure 4.3. As the spheres go from nearly perfectly close packing density (Figure 4.2 a) to a packing density of 35% (Figure 4.2 e), minima in the diffuse reflection form at a wavelength of about 600nm and a maxima form at a wavelength of about 1100RPM. This is similar to the maximum and minimum points found in the research and simulations by P. Jiang et al.(15). The smoothing of the reflection peak and valley is presumed to be due to the lack of a long range order but this should be verified by simulation. The optimum diffuse reflection occurs for a packing density of 35% which corresponds to a 4000RPM spin rate. For lesser densities, the diffuse reflection begins to decrease and becomes specular reflection. This was expected because the planar substrate is being revealed. It should be noted that a packing density of 0% would be a flat silver substrate with nearly 100% specular reflection.

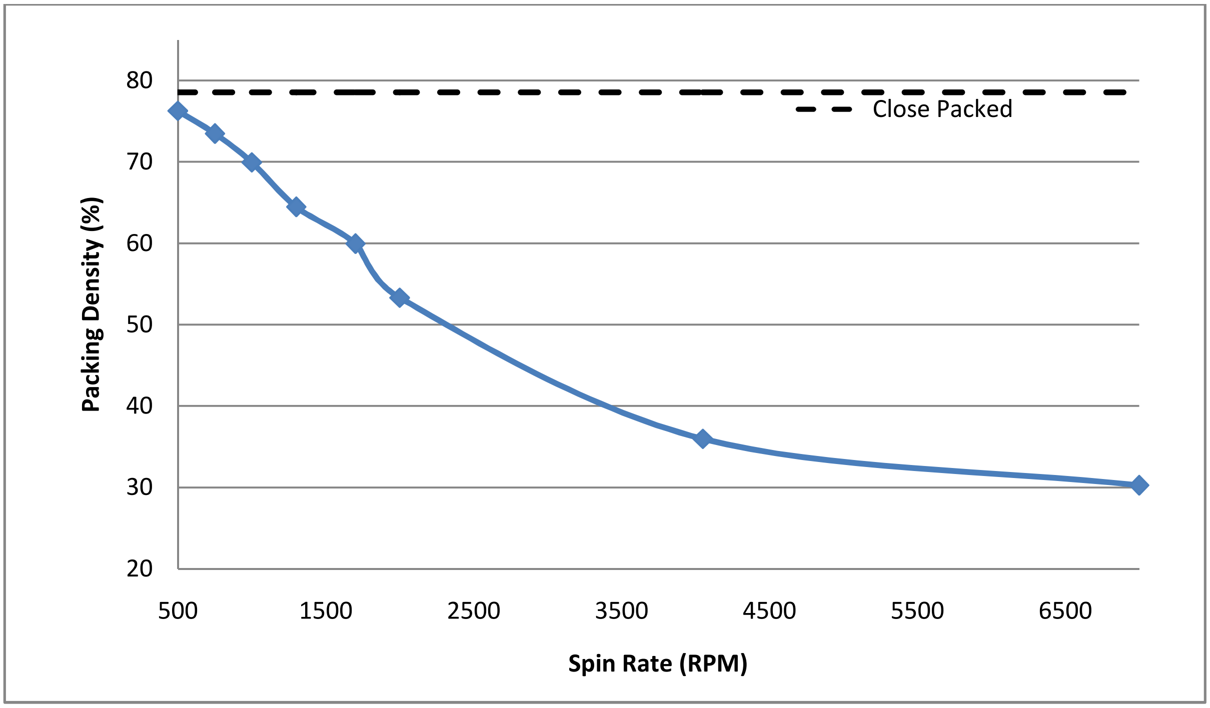

**Figure 4.1. Percentage packing density versus spin coating rate for 500nm sphere substrates (close packed density given for reference)**

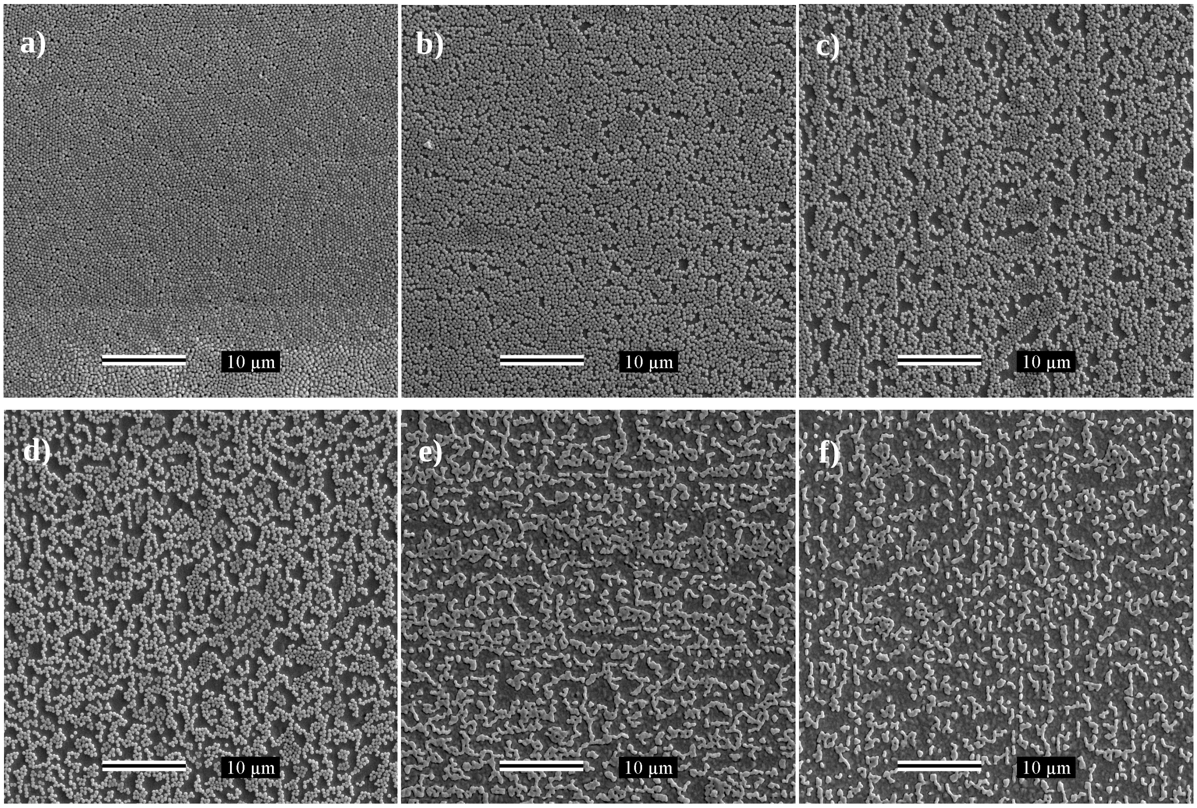

**Figure 4.2. SEM images of 500nm sphere back reflectors spin coated at a) 500RPM, b) 1000RPM, c) 1700RPM, d) 2000RPM, e) 4050RPM, and f) 7000RPM illustrating the packing density**

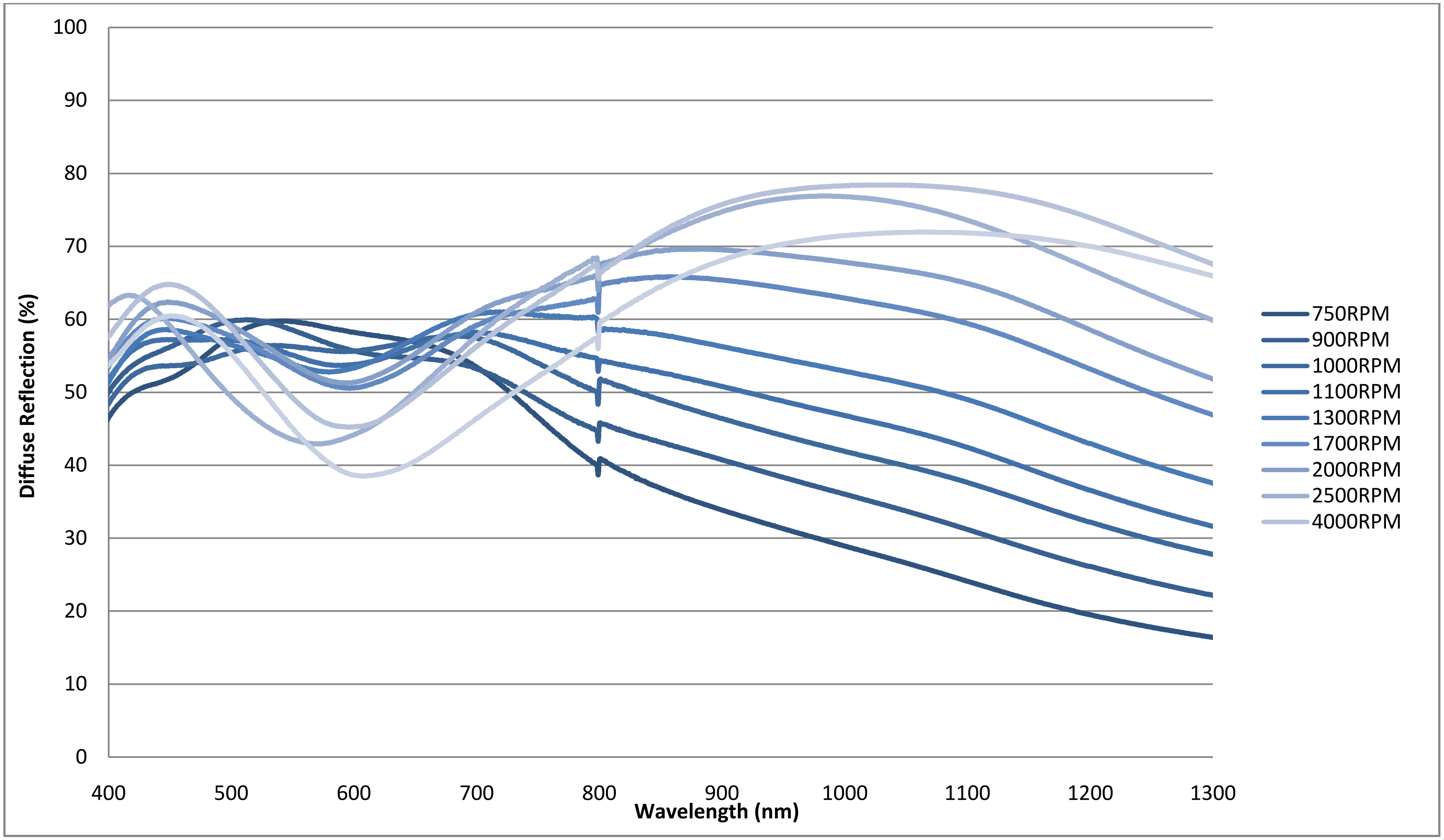

**Figure 4.3 Diffuse reflection versus wavelength for various spin rates (750RPM to 4000RPM) for 500nm sphere colloid**[2]

---

[2] The discontinuity in the diffuse reflection at a wavelength of 800nm is cause by a detector and grating changeover

### 4.1.2 250nm Silica Sphere Back Reflectors

In this section, diffuse reflection results are given for stainless steel substrates textured with 250nm silica spheres and coated with 150nm of silver. The substrates were prepared with the methodology presented in Chapter 2. A sweep of the spin coating rate from 500RPM to 10000RPM was performed. Contrary to the results for the 500nm silica spheres, monolayers were not formed for all spin rates. Figure 4.5 a) and b) show back reflectors with multilayers of 250nm spheres prepared by spin coating rates of 500RPM and 1000RPM, respectively. The back reflector in Figure 4.5 c) shows a close packed sphere monolayer generated at a spin rate of 1700RPM. This indicates the minimum spin rate to produce a monolayer of spheres. For 500nm spheres, this spin rate was around 500RPM. Considering only kinetics, it should require a lesser centripetal force to spread smaller/lighter spheres. This is not the case because particles at these dimensions are dominated by the van der Waals force which is stronger for the 250nm spheres. Figure 4.5 d-f) show back reflectors with decreasing packing density for increases spin rate, as expected. Figure 4.4 is a plot of the packing density (found using the method in the Appendix) versus the spin rate. For spin rates less than 1700RPM the packing density saturates at the close packing density as expected.

The diffuse reflection for these substrates is shown in Figure 4.6. There is a trend very similar to that seen for the diffuse reflection of the 500nm back reflectors in Figure 4.3. For close packing and multilayers, it appears that a peak is forming at around 300nm. Unfortunately, silver reflection begins to give way to transmission at wavelengths around 450nm so a peak is formed early at around 480nm. A peak is again formed at a little more than twice the diameter of the spheres at about 650nm for low packing densities. Also, the reflection at 400nm begins to decrease for decrease packing densities, possibly indicating the formation of a minimum at around 300nm. Unfortunately, the data does not extend to low enough wavelengths to make a suitable conclusion.

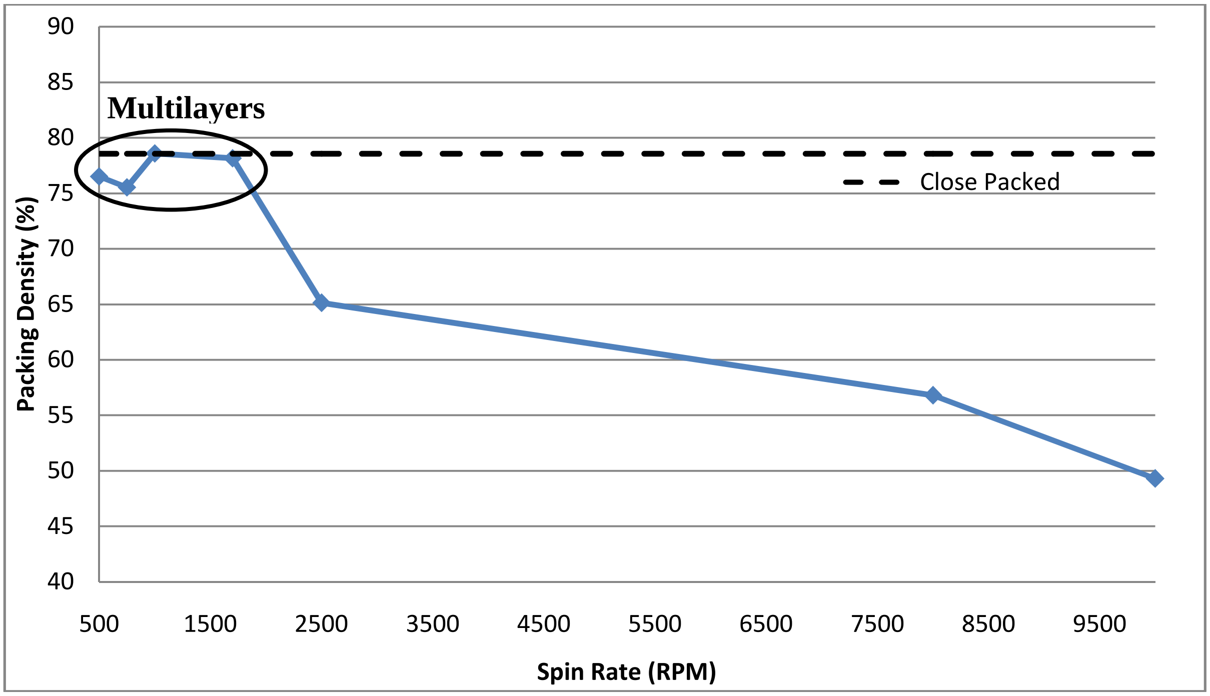

**Figure 4.4. Percentage packing density versus spin coating rate for 250nm sphere substrates (close packed density given for reference)**

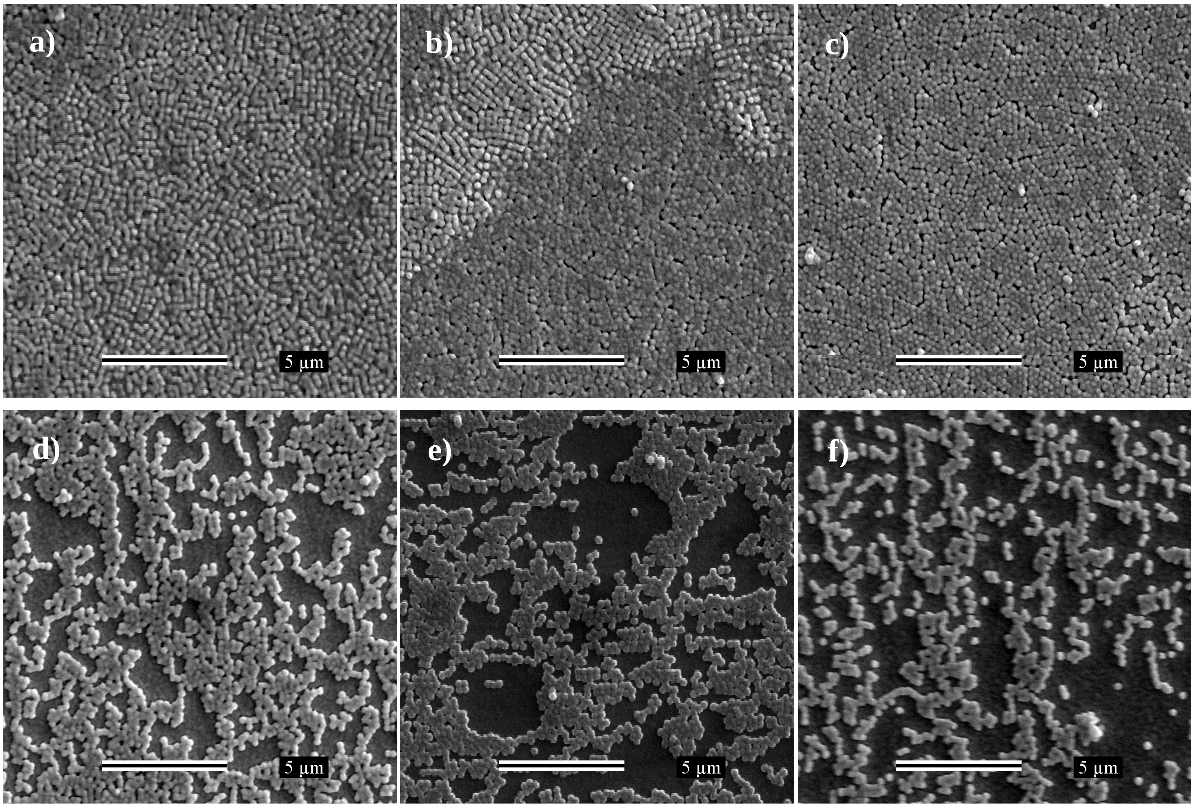

**Figure 4.5. SEM images of 250nm sphere back reflectors spin coated at a) 500RPM, b) 1000RPM, c) 1700RPM, d) 2500RPM, e) 8000RPM, and f) 10000RPM illustrating the packing density**

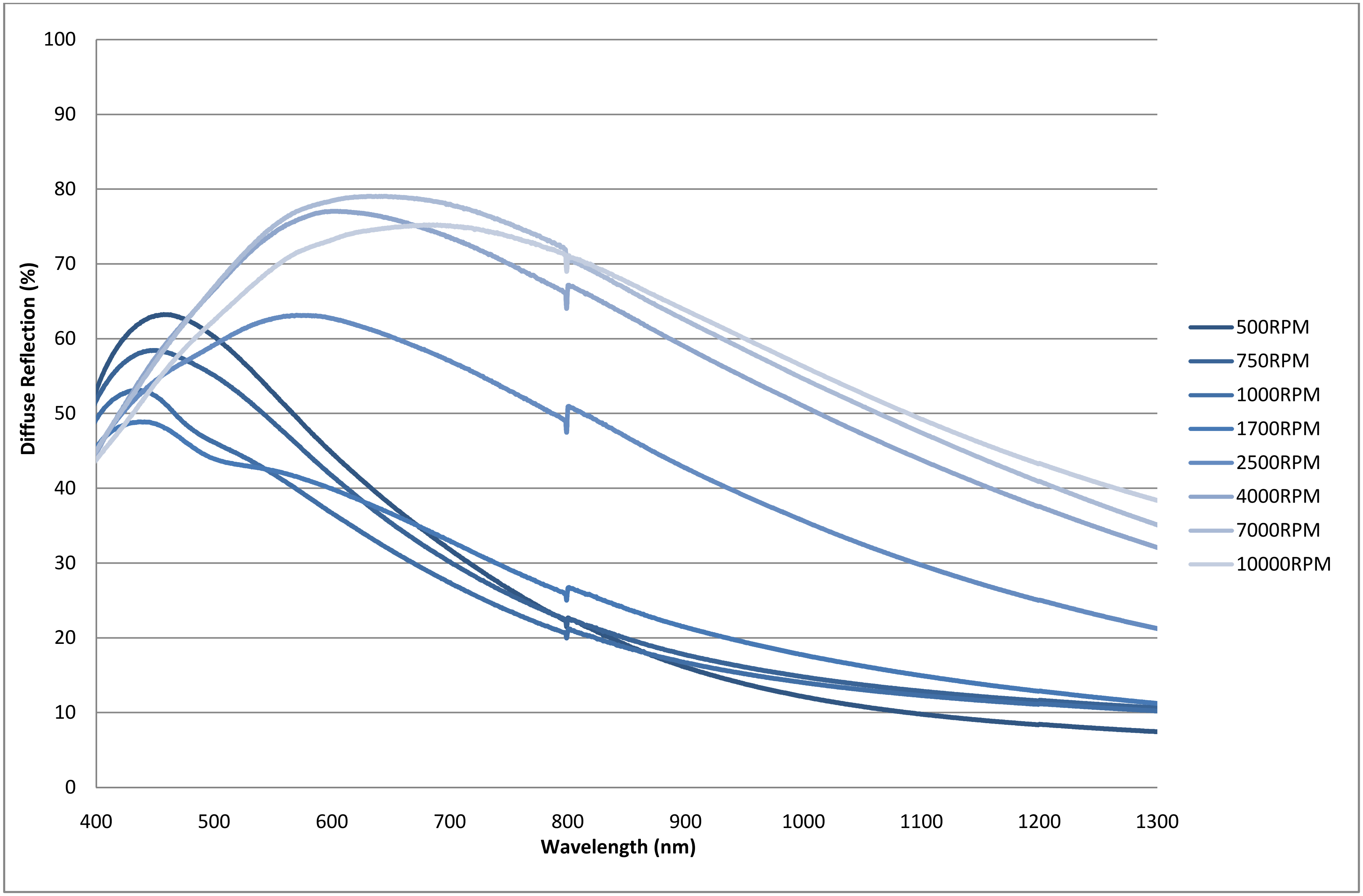

**Figure 4.6 Diffuse reflection versus wavelength for various spin rates (500RPM to 10000RPM) for 250nm sphere colloid**

The peak diffuse reflection in Figure 4.6 is 80% and is for a substrate spin coated with 250nm spheres at 7000RPM and coated with 150nm of silver. Figure 4.7 shows the total, diffuse, and specular reflection of a similar substrate spin coated at 8000RPM. The total reflection is just greater than 80%, which was not expected for 150nm of silver. This decrease in total reflection is attributed to the shadowing effect of the silver evaporation. The spheres shadow the substrate from silver, and the sides of the silica spheres are not initially coated with silver. Therefore, there are areas of the back reflector that absorb light. Thicker layers of silver were necessary to lessen this reflection loss. Figure 4.7 gives the total, specular, and diffuse reflection for three substrates spin coated at 8000RPM and coated with 150nm, 250nm, and 300nm of silver. The peak total reflection was nearly 95% and 300nm was determined to be the point of diminishing returns. The solid line reflection plot in Figure 4.7 corresponds to the reflexivity of the substrate used for all solar cell devices built on 250nm sphere back reflectors.

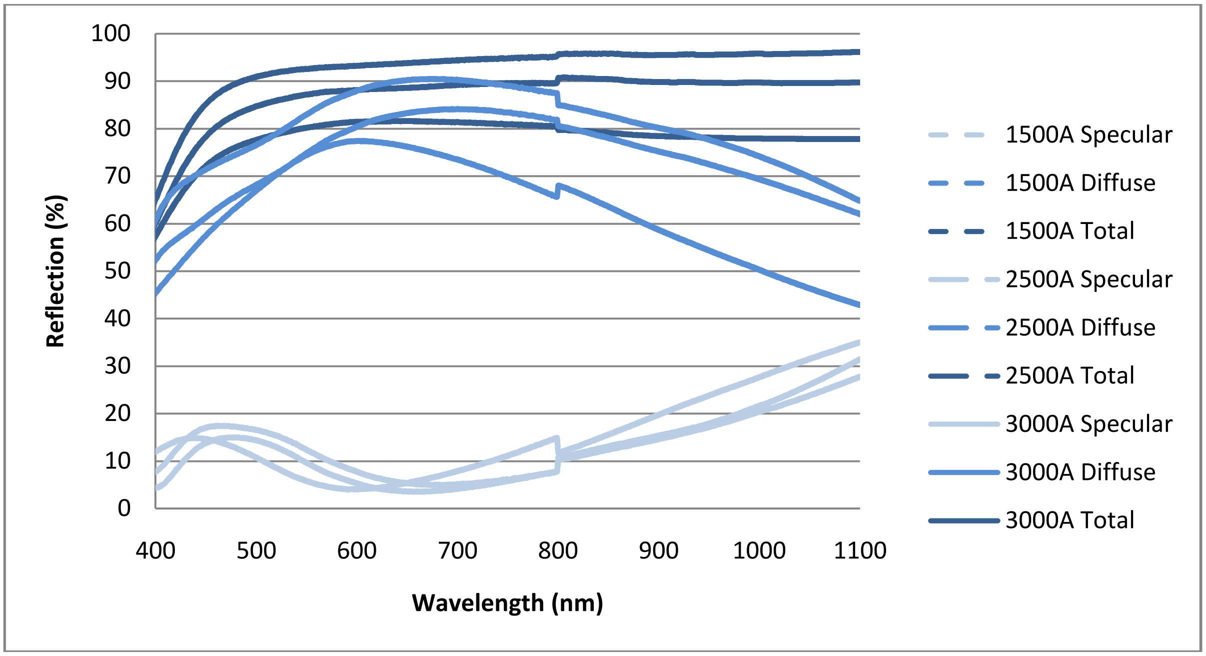

**Figure 4.7. Total, specular, and diffuse reflection for 250nm sphere back reflectors coated with 1500Ǻ, 2500Ǻ, and 3000Ǻ**

Aluminum coated spheres were considered as a substrate for a-Si:H solar cells. Figure 4.8 is a plot of the total, specular, and diffuse reflection of 300nm of aluminum on 250nm spheres spin coated at 8000RPM. Aluminum transmits light at a wavelength of around 850nm, which can be observed in the dip of total reflection at this point. For this reason aluminum coated back reflectors are sufficient for a-Si cells because the band gap is 1.6 to 1.8eV which implies that most photons of wavelengths greater than 775nm will never be absorbed. This dip in reflection is problematic for nc-Si solar cells which have a band gap of 1.12eV and can absorb light up to a wavelength of 1100nm. Also, the total reflection of aluminum is less than that of silver. It is believed that the aluminum back reflector would be a feasible alternative to the silver reflector, but no devices were made to confirm this postulation.

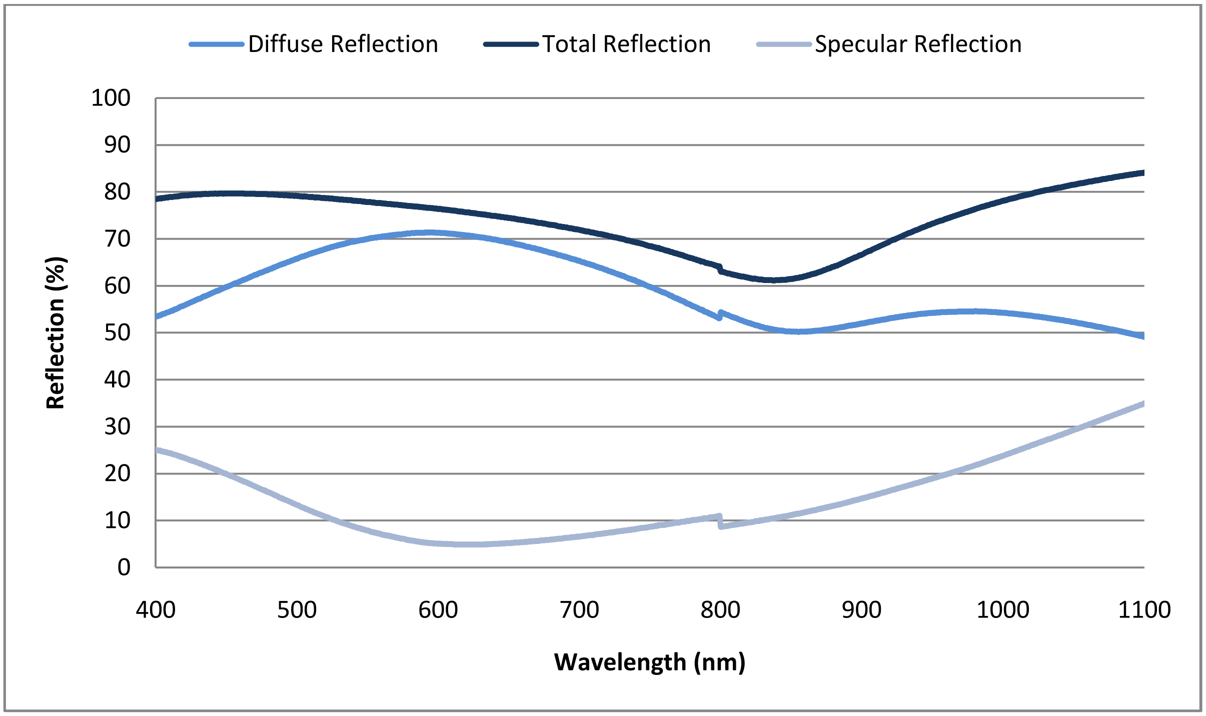

**Figure 4.8. Total, specular, and diffuse reflection of 300nm of aluminum on 250nm spheres spin coated at 8000RPM**

## 4.2 Nanocrystalline Silicon Devices

Four nc-Si:H devices were built on 250nm sphere substrates spin-coated at 8000RPM coated with 300nm of silver. The devices were built with a target intrinsic layer thickness of 1.5μm (see Figure 2.8 and accompanying discussion for other device dimensions). Figure 4.9 a) shows an SEM image of the nc-Si device 1-6798 built on a 250nm sphere back reflector. The silicon tends to collect around the spheres, and there are defects in the solar cell structure. Figure 4.9 b) shows the same device looking down on an ITO contact. Due to the total thickness of the nc-Si films, shorting was not found to be a problem in device testing.

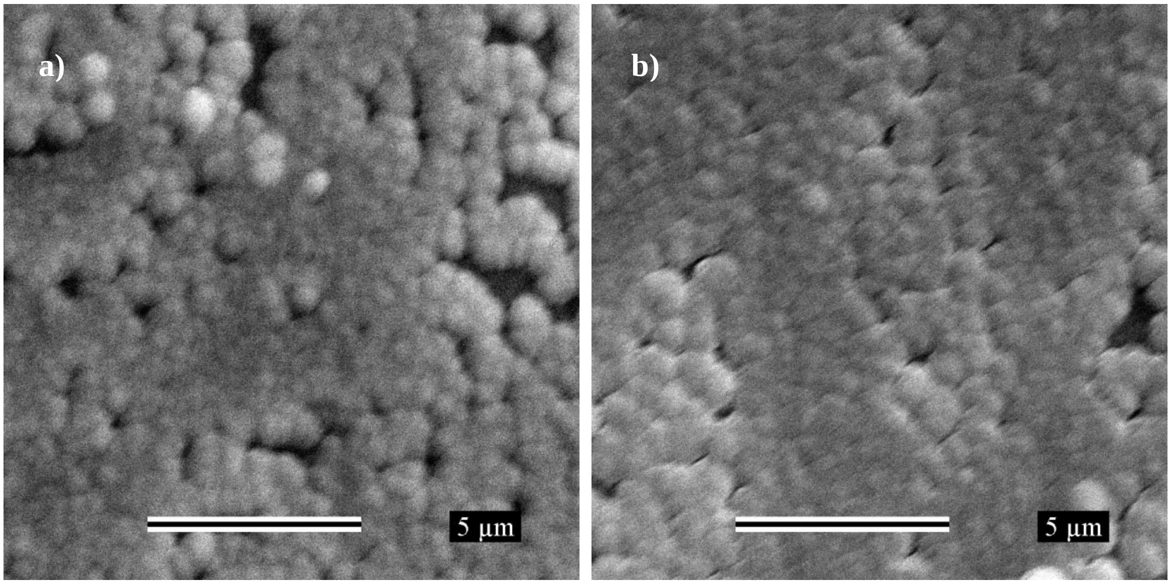

**Figure 4.9. SEM images of a) a nc-Si solar cell (1-6798) on 250nm sphere back reflector and b) the same solar cell looking down on the ITO contact**

The performance of the first device (1-6798) degraded significantly after an ITO anneal step and therefore QE data was not collected. This step was subsequently removed from the process. Before the anneal, I-V data was collected and the $V_{OC}$ was 0.447V, $I_{SC}$ was 2.17mA, and FF was 49.4. Three other devices were made without performing an ITO anneal, and the normalized QE for these devices are shown in Figure 4.10 and Figure 4.11 with 0V and -0.5V applied biases, respectively.

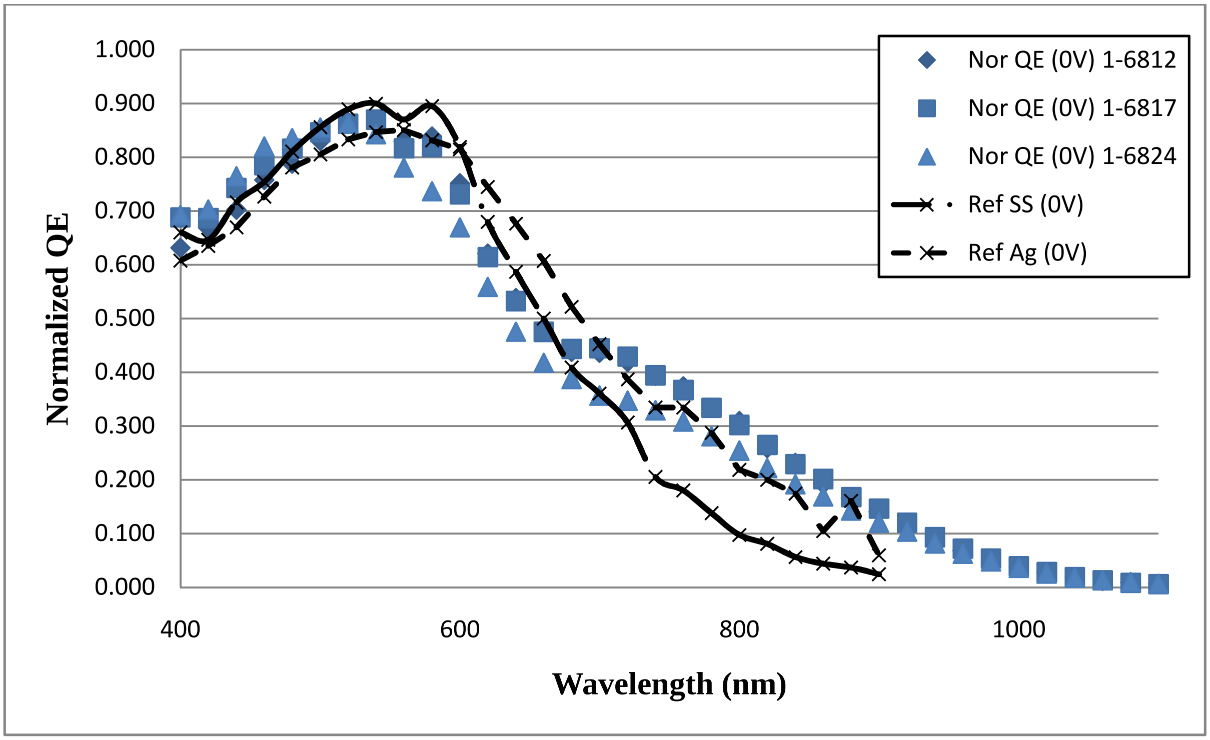

**Figure 4.10. Normalized quantum efficiency (Vbias=0V) for three nc-Si:H devices (1-6812,1-6817, and 1-6824) on 250nm sphere back reflectors. Devices on SS and Ag substrates plotted for reference.**

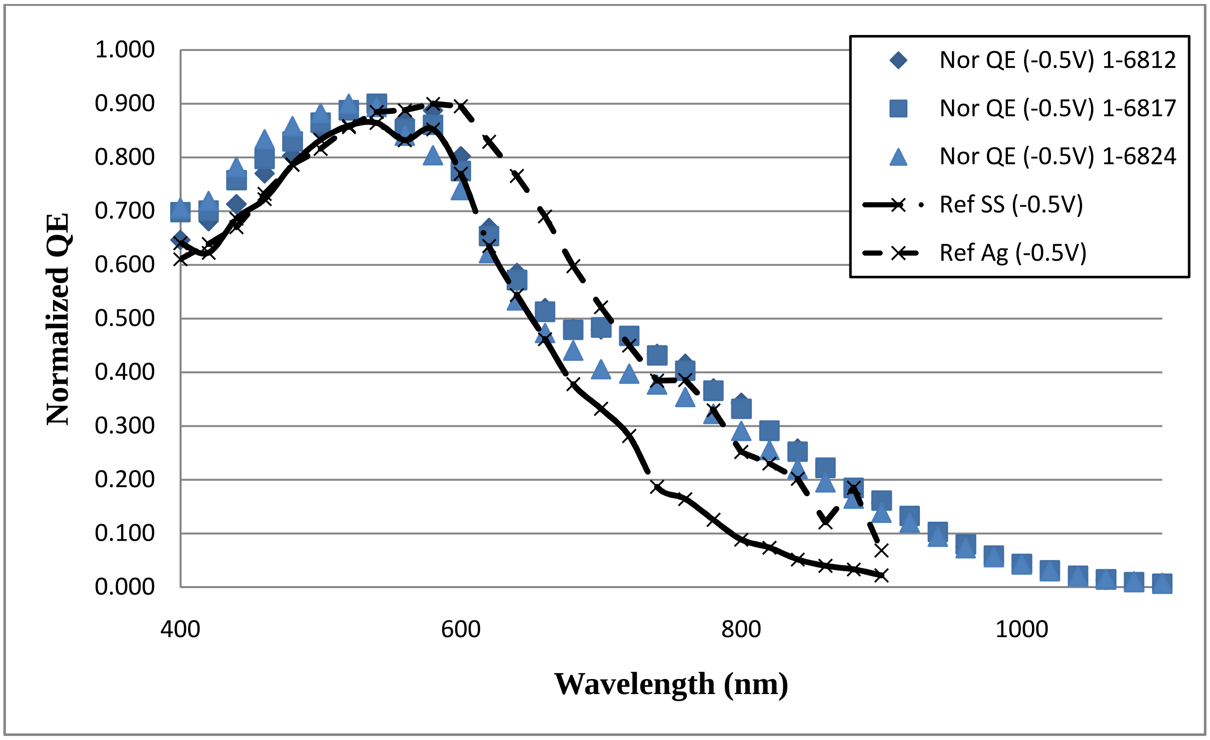

**Figure 4.11. Normalized quantum efficiency (Vbias=-0.5V) for three nc-Si:H devices (1-6812,1-6817, and 1-6824) on 250nm sphere back reflectors. Devices on SS and Ag substrates plotted for reference.**

Included in the QE plots in Figure 4.10 and Figure 4.11 are reference devices built on a bare stainless steel substrate (SS) and on 500Ǻ of silver on a SS substrate. Figure 4.12 shows the ratio of each device QE to the QE of the SS and Ag reference substrates. From this normalization is it clear that a significant portion of the enhancement over the SS substrate comes from the highly reflective property of silver: there is a factor of 7 increase at 900nm over the device on SS and only a factor of 2 increase over the device on Ag. Silver tends to agglomerate at the high temperatures and moderate pressures that the substrate is exposed to during the growth of the solar cell. It is suspected (but not experimentally verified) that the silver agglomerated on the substrate and increased the diffuse reflection. Regardless of this, the factor of 2 improvement at 900nm demonstrates a significant increase in light trapping.

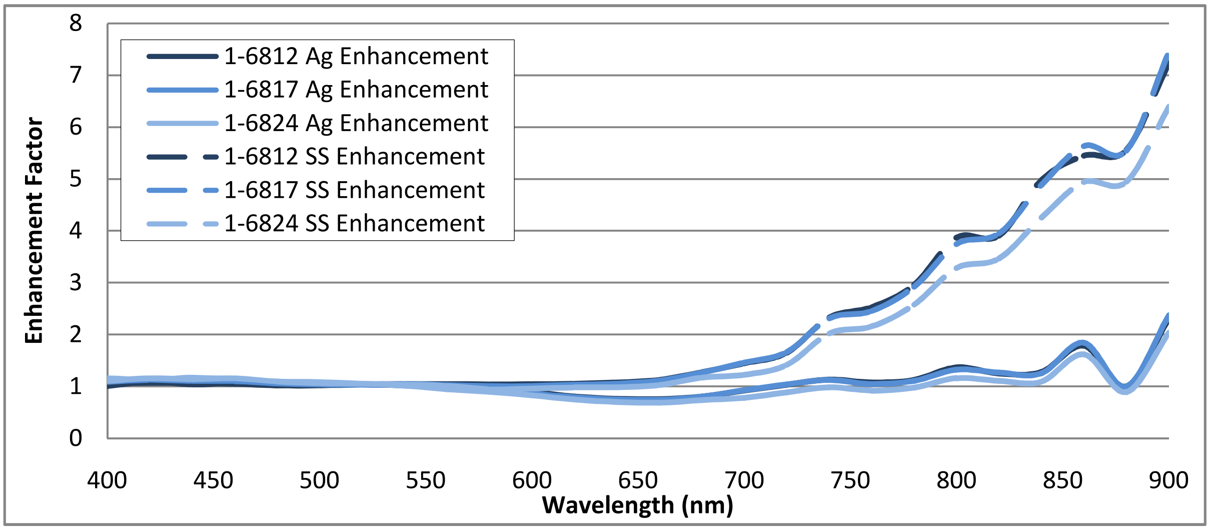

**Figure 4.12. QE enhancement ratios for devices 1-6812, 1-6817, and 1-6824. Enhancement over SS reference as dashed curves and enhancement over Ag as solid curves.**

A summary of the characteristics of the nc-Si solar cells built on the 250nm back reflectors is given in Table 4.1 along with the parameters of the reference devices. The devices showed an average increase in short circuit current of 5% as compared to the SS reference but a decrease of 4.3% as compared to the Ag reference. The average $J_{SC}$ (measured by summing current in the QE) showed a 15% increase over the SS reference but showed no appreciable change as compared to the Ag reference.

**Table 4.1. Summary of device characteristics for nanocrystalline solar cells and reference cells**

| Device | Substrate | $V_{OC}$ (V) | $I_{SC}$ (mA) | FF | QE ratio to SS at 900nm | QE ratio to Ag at 900nm | $J_{SC}$ from QE (mA/cm$^2$) |
|---|---|---|---|---|---|---|---|
| 1-6798 | 250nm BR | 0.447 | 2.17 | 49.4 | - | - | - |
| 1-6812 | 250nm BR | 0.474 | 2.25 | 45.1 | 7.24 | 2.31 | 17.46 |
| 1-6817 | 250nm BR | 0.475 | 2.28 | 50.4 | 7.45 | 2.37 | 17.58 |
| 1-6824 | 250nm BR | 0.4679 | 2.025 | 53.7 | 6.39 | 2.04 | 16.32 |
| 1-6808 | SS | 0.4705 | 2.077 | 34.1 | 1 | 0.3189 | 14.87 |
| 1-6838 | SS/500Ǻ Ag | 0.4939 | 2.276 | 53.3 | 3.136 | 1 | 17.34 |

## 4.3 Amorphous Silicon Devices

### 4.3.1 Devices on 500nm Sphere Back Reflectors

Four a-Si:H devices were built on spin-coated 500nm sphere substrates with 150nm of silver. The first two substrates were spin coated at 500RPM (2-11925 and 2-11961) and the second two at 1300RPM (2-12006 and 2-12035). It should be noted that these were not determined to be the optimum back reflectors from diffuse reflections measure, but the test bench to measure diffuse reflection was not operational at the time that these devices were made. These back reflectors were chosen for their close-packed characteristics without any spectrum data.

The devices were built with a target intrinsic layer thickness of 0.25 µm (see Figure 2.7 and accompanying discussion for other device dimensions). Device shorting was a frequent problem during testing and characterization likely due to the fact that the dimensions of the device were on the order of the dimensions of the features of the back reflector. Figure 4.13 shows an optical micrograph at 40X magnification of the ITO contact of an a-Si solar cell built on a 500nm sphere substrate. The image is focused on a short that occurred from placing a contact during device testing. Another thing to note from the image are the defects in the solar cell structure. These areas were determined by SEM imaging to be areas with no silica spheres. This issue was resolved by cleaning the SS substrates before spin coating as detailed in Chapter 2. This cleaning step was performed on all of the substrates other than those presented in this section.

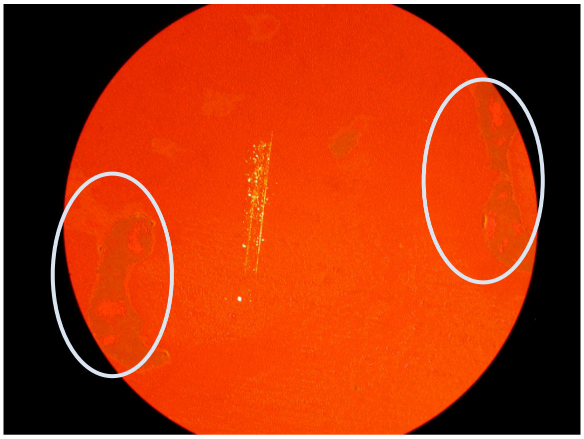

**Figure 4.13. Optical micrograph (40X) the ITO contact of an a-Si solar cell displaying a short developed during characterization. Defects identified with ovals.**

Figure 4.14 a) shows an SEM image of the a-Si device 2-11961 built on a 500nm sphere back reflector. The silicon tends to group around the spheres and there are empty patches in the solar cell structure. Figure 4.14 b) shows the same device looking down on an ITO contact. The coverage of the features of the back reflector is significantly less than that of the nc-Si device as seen in Figure 4.9. It is easy to imagine a probe tip penetrating this surface, resulting in a short like that displayed in Figure 4.13.

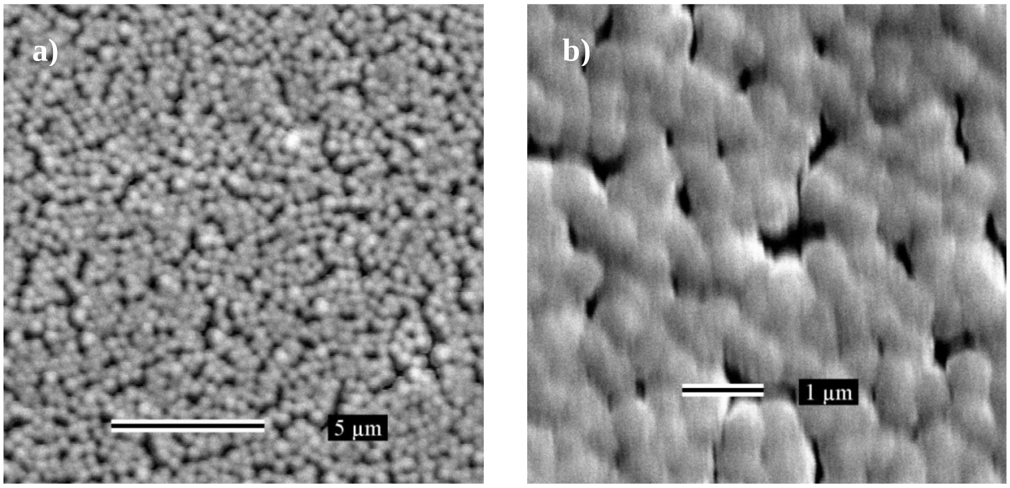

**Figure 4.14. SEM images of a) a-Si solar cell (2-11961) on a 500nm sphere back reflector and b) the ITO on the same solar cell**

The normalized QEs of devices 2-11961, 2-12006, and 2-12035 for a 0V applied bias are shown in Figure 4.16. The normalized QE plot at a 0.5V bias (Figure 4.17) only shows the data for 2-11961 and 2-12035 because 2-12006 shorted during testing. The reference device (2-12119B) in both Figure 4.16 and Figure 4.17 was built with the same device parameters but on a SS substrate. Although each back reflector and solar cell device was fabricated identically, there is a significant decrease in the QE enhancement at longer wavelengths for device 2-12006 as compared to 2-11961 as well as 2-12035 as compared to 2-12006. All of the devices were fabricated in reactor 2 which became contaminated due to silicon germanium experiments that were being performed in parallel to this research. This contamination is attributed to the degradation in solar cell device performance.

Figure 4.15 shows the QE enhancement ratio of the devices to the stainless steel reference device. The peak enhancement ratio occurs at a wavelength of 760nm and is about 9.42 for device 2-11961, 5.6 for device 2-12006, and 3.88 for device 2-12035. Other device parameters are summarized along with data for amorphous devices on 250nm back reflector in Table 4.2.

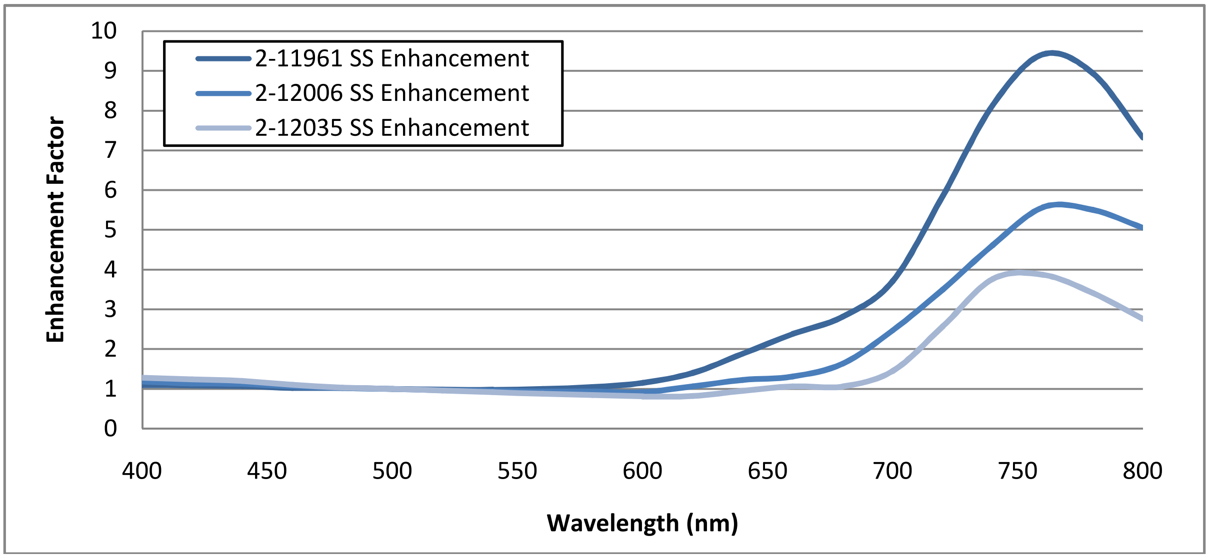

**Figure 4.15. QE enhancement ratios over SS substrate for devices 2-11961, 2-12006, and 2-12035 for a 0V applied bias**

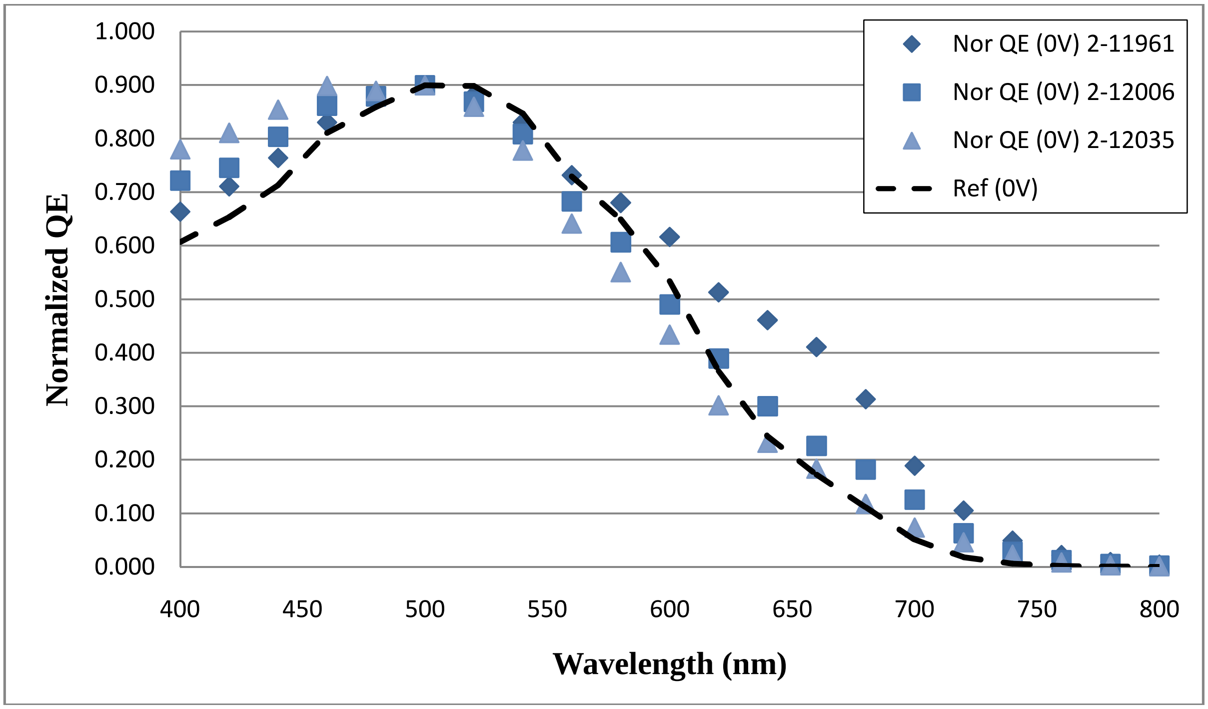

**Figure 4.16. Normalized quantum efficiency (Vbias=0V) for three a-Si:H devices (2-11961, 2-12006, and 2-12035) on 500nm sphere back reflectors and a reference device (2-12119B) on a stainless steel substrate**

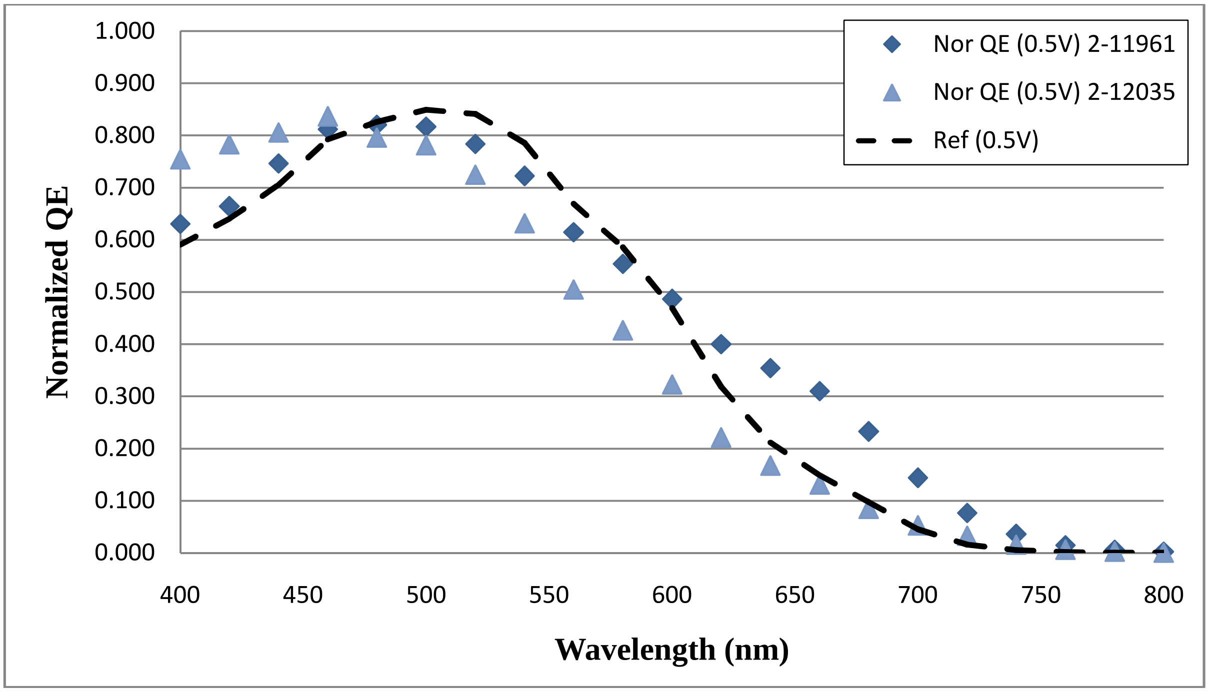

**Figure 4.17. Normalized quantum efficiency (Vbias=0.5V) for two[3] a-Si:H devices (2-11961 and 2-12035) on 500nm sphere back reflectors and a reference device (2-12119B) on a stainless steel substrate**

---

[3] The 0.5V applied bias QE for 2-12006 is not presented here because the device shorted during testing

### 4.3.2 Devices on 250nm Sphere Back Reflectors

Three a-Si devices were built on 250nm sphere substrates spin-coated at 8000RPM coated with 300nm of silver. The devices were built with a target intrinsic layer thickness of 0.25 µm (see Figure 2.7 and accompanying discussion for other device dimensions). Device shorting was a frequent problem during testing and characterization just as it was for the amorphous devices on the 500nm sphere back reflectors. It is conceivable that an amorphous device with a thicker n+ layer or intrinsic layer could be designed to eliminate this issue, but this was considered to be beyond the scope of this project.

Device data was collected for two of the three devices by using great care in placing the probe contacts similar to the way data was collected for amorphous devices on 500nm spheres. Device 2-12152 was shorted on all 9 contacts made and no data was able to be collected for this cell. Figure 4.18 a) shows an SEM image of the device 2-12110. Figure 4.18 b) is an SEM image of the ITO contact of the same device. It is easy to imagine a probe tip penetrating this surface just like the surface of the device on 500nm spheres in Figure 4.14.

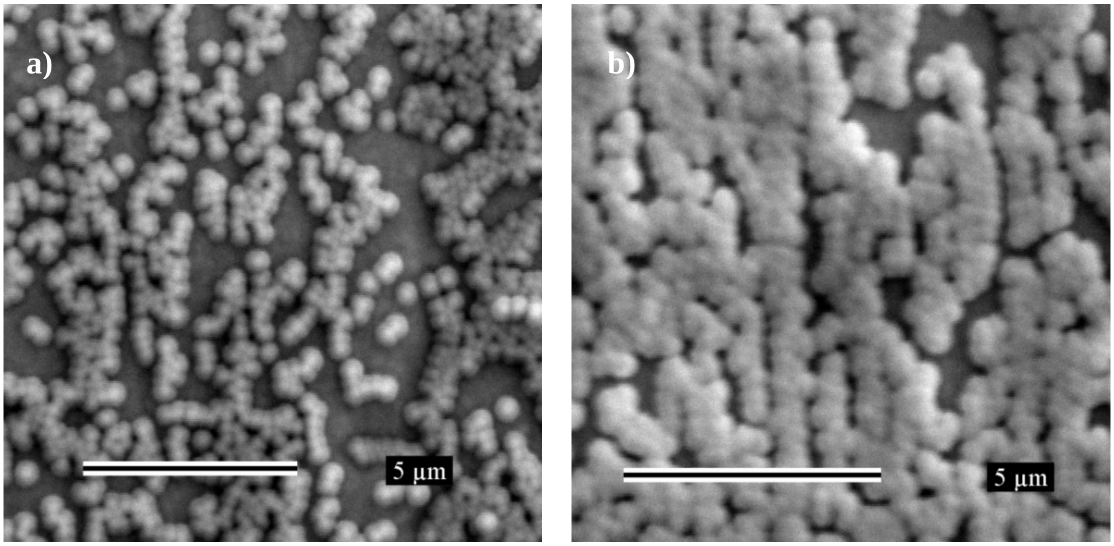

**Figure 4.18. SEM images of a) a-Si solar cell (2-12110) on a 250nm sphere back reflector and b) the same solar cell looking down on the ITO contact**

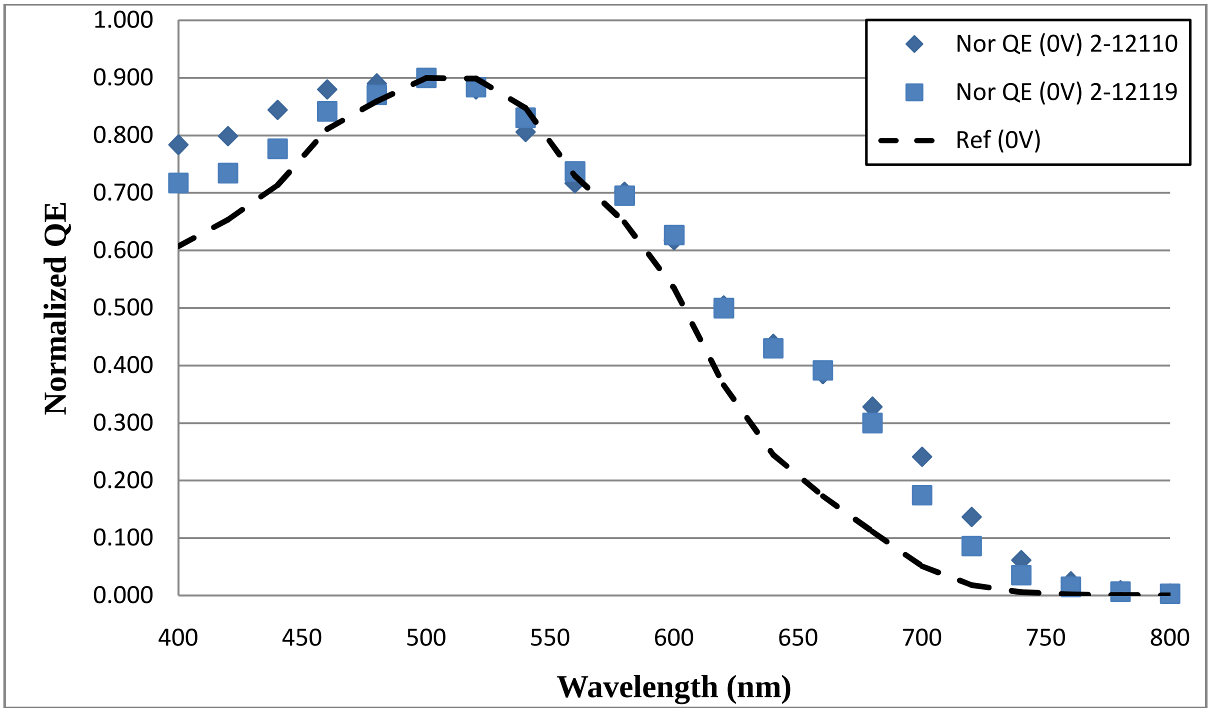

**Figure 4.19. Normalized quantum efficiency (Vbias=0V) for two a-Si:H devices (2-12110 and 2-12119) on 250nm sphere back reflectors and a reference device (2-12119B) on a stainless steel substrate**

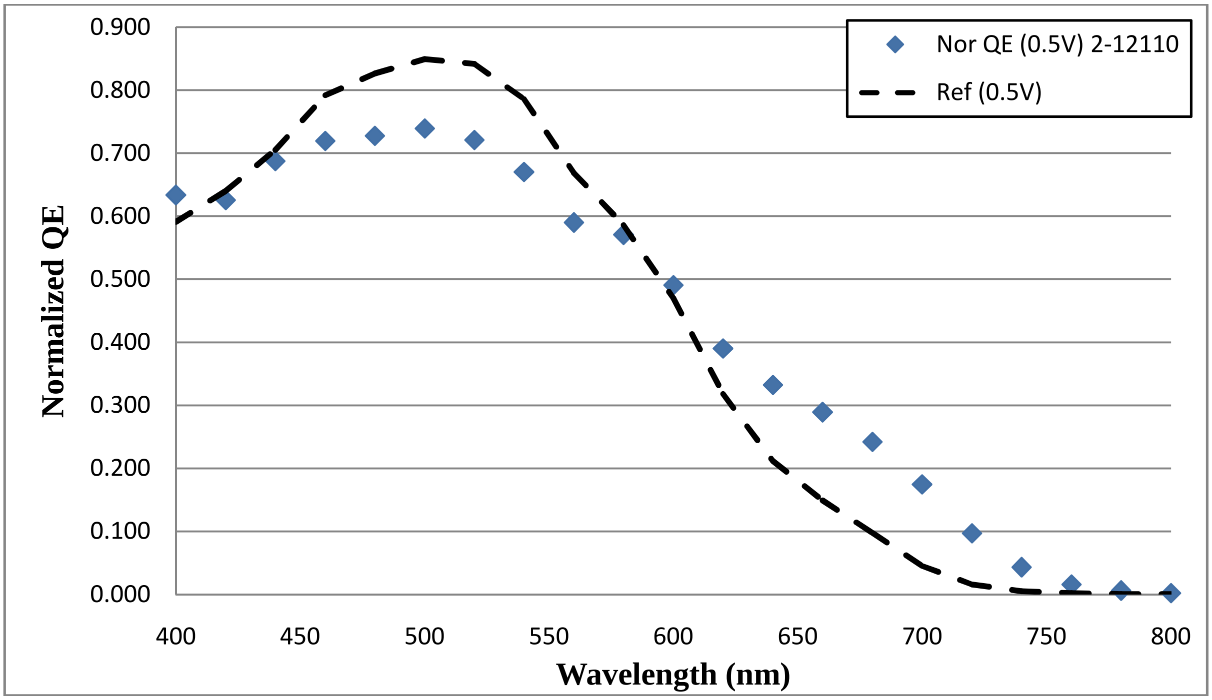

**Figure 4.20. Normalized quantum efficiency (Vbias=0.5V) for an a-Si:H devices (2-12110[4]) on 250nm sphere back reflectors and a reference device (2-12119B) on a stainless steel substrate**

---

[4] The 0.5V applied bias QE for 2-12110 is not presented here because the device shorted during testing

The normalized QEs of devices 2-12110 and 2-12119 for a 0V applied bias are shown in Figure 4.19. The normalized QE plot at a 0.5V bias (Figure 4.20) only shows the data for 2-12110 because device 2-12119 shorted during testing. The reference device (2-12119B) in both Figure 4.19 and Figure 4.20 was built with the same device parameters but on a SS substrate. It is the same device as the reference used in Figure 4.16 and Figure 4.17 for devices on 500nm sphere back reflectors. The improvement in QE at wavelengths greater than 600nm was significant for both devices. The peak enhancement occurs at 760nm and was 10.5 for device 2-12110 and was 6.6 for 2-12119. Other device parameters are summarized along with data for amorphous devices on 250nm back reflector in Table 4.2.

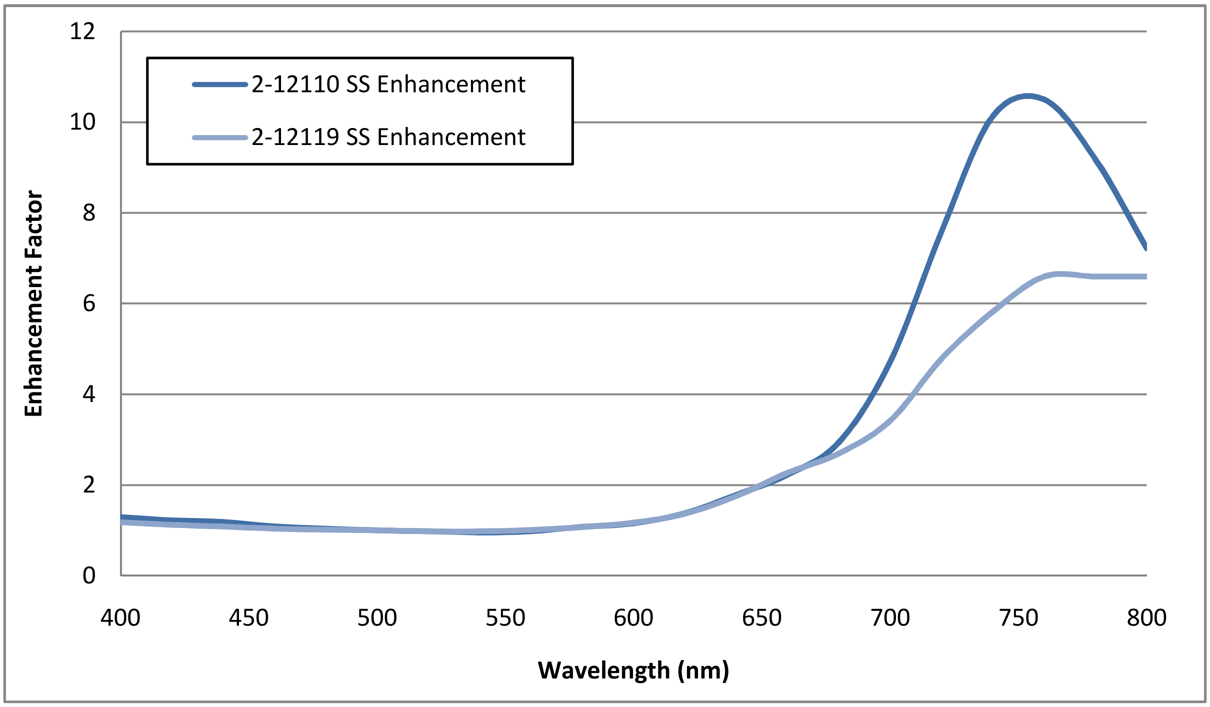

**Figure 4.21. QE enhancement ratios over SS substrate for devices 2-12110 and 2-12119 for a 0V bias**

Table 4.2 summarizes the device characteristics for all amorphous silicon solar cells fabricated on nanosphere back reflectors in this research. Device 2-11925 shorted due to a lack of a post-anneal after the spin coating of the spheres. This was discussed in greater detail in Chapter 2. It should once again be noted that 2-12006 and 2-12035 were fabricated while reactor 2 was contaminated and the degradation in performance of these devices is attributed to this. Devices 2-11961, 2-12110, and 2-12119 had an average increase in short circuit current over the stainless steel reference of 27%; an average increase in $J_{SC}$ (found by summing currents from the QE measurement) of 18%; and an average maximum enhancement factor of 8.84 at 760nm.

**Table 4.2. Summary of device characteristics for amorphous solar cells and reference cells**

| Device | Substrate | $V_{OC}$ (V) | $I_{SC}$ (mA) | FF | QE ratio to SS at 760nm | $J_{SC}$ from QE (mA/cm$^2$) |
|---|---|---|---|---|---|---|
| 2-11925 | 500nm BR | All contacts shorted. | | | | |
| 2-11961 | 500nm BR | 0.775 | 1.32 | 52.2 | 9.42 | 12.9 |
| 2-12006 | 500nm BR | 0.679 | 1.01 | 56.2 | 5.57 | 11.56 |
| 2-12035 | 500nm BR | 0.716 | 1.03 | 56 | 3.41 | 10.99 |
| 2-12110 | 250nm BR | 0.755 | 1.36 | 51 | 10.49 | 13.23 |
| 2-12119A | 250nm BR | 0.751 | 1.36 | 59.2 | 6.60 | 12.82 |
| 2-12152 | 250nm BR | All contacts shorted. | | | | |
| 2-12119B | SS Ref | 0.829 | 1.06 | 62.8 | 1 | 11 |

# CHAPTER 5. CONCLUSIONS AND FUTURE WORK

The objective of this research was to design a back reflector to increase light trapping in amorphous and nanocrystalline silicon solar cells. This was completed by using texturing substrates with silica nanospheres. Back reflectors were fabricated with 250nm and 500nm spheres and exhibited peaks in diffusion reflection at wavelengths of 650nm and 1050nm, respectively. These peaks were determined to be due to the constructive interference Bragg diffraction of the non-close packed spheres, and their smooth characteristic was presumed to be due to the lack of long-range order. Future work would include simulating the back reflector and fabricating substrates with 350nm silica spheres. The latter should shift the peak in diffuse reflection to the optimum wavelength of about 750nm.

Nanocrystalline devices built on the 250nm back reflectors showed substantial increases in quantum efficiency over similar devices built on stainless steel substrates. A factor of two increase in QE at 900nm as compared to a device on a silver coated substrate was also observed. With careful probe placement, sufficient data was also collected from amorphous silicon devices to measure an increased carrier collection as compared to a similar device built on a stainless steel substrate. Future work is necessary to design an amorphous device with an increased n+ layer thickness to prevent frequent contact shorting.

Other future work would include designing an industrially scalable nanosphere deposition technique. Spin coating is not a feasible process for the dimensions of the solar cells fabricated in industry. One possible solution would be to use pull coating at a rate which deposits spheres with the same packing density achieved in this research.

# APPENDIX. PACKING DENSITY CHARACTERIZATION

For this project, a MATLAB script was written and used to characterize the packing density of spheres on a substrate. The script takes advantage of the contrast between the silica spheres and the substrate in the SEM images. This contrast can be seen in Figure 5.1 a). The code for the MATLAB m-file is given in Figure 5.2. The script works by reading in the SEM image to a 256-bit grayscale matrix with the size determined by the image resolution using the imread() function. The SEM image resolution can be set during acquisition and the user must specify this same resolution in the script. A value is then set at the midpoint between the average grayscale value of the sphere area of the image and the average grayscale value of the substrate area of the image. A loop then checks each pixel to see if its value is greater than this grayscale value. If the pixel value is greater than this point, it is considered to be a sphere pixel. The total number of sphere pixels is divided by the total number of pixels in the image and printed out as the packing density. Also, an image is generated with the sphere pixels in white and substrate pixels in black like the image in Figure 5.1 b). This image helps to determine if the set point is correct and if the sphere/substrate contrast is sufficient.

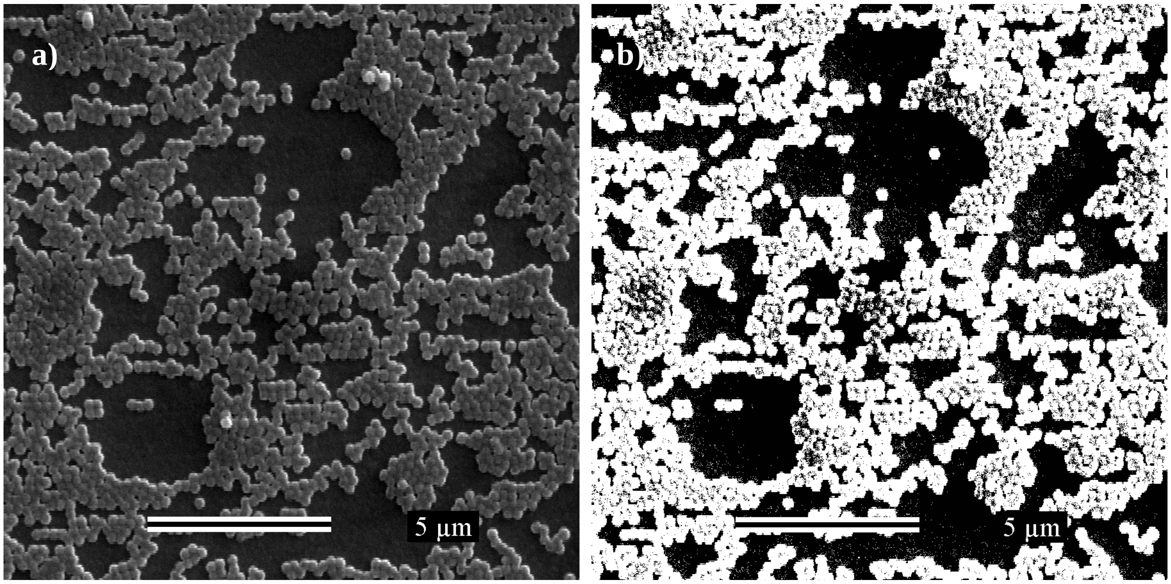

**Figure 5.1. a) SEM image of a back reflector and b) image output from MATLAB script**

```
%image resolution
xPIXELS=900;
yPIXELS=900;

%input file name
I=imread('filein.TIF');

%cutoff point for sphere pixel given as a percentage of the average value
%of the image
N=mean(mean(I))*0.8

%initialize variables
Ibw=I;
totWhite=0

%loop for every pixel in image
for i=1:xPIXELS
    for j=1:yPIXELS
        %if pixel is brighter than cutoff pixel, set output image pixel
        %to white and add one to sphere pixel count else set to black
        if (I(i,j)>N)
            Ibw(i,j)=256;
            totWhite=totWhite+1;
        else
            Ibw(i,j)=1;
        end
    end
end

%normalize sphere pixel count to total number of pixels
totWhite=100*totWhite/(xPIXELS*yPIXELS)

%show image with percentage packing density in title
imshow(Ibw1);
title([num2str(totWhite) '%'])

%save and close image
saveas(gcf,['./Results/filein.pdf'])
close
```

**Figure 5.2. MATLAB m-file script used to characterize the silica sphere packing density**

# BIBLIOGRAPHY

1. *Material and solar cell research in microcrystalline silicon.* **Shah, A.V., et al.** 1-4, s.l. : Solar Energy Materials and Solar Cells, 2003, Vol. 78.

2. *Improving thin-film crystalline silicon solar cell efficiencies with photonic crystals.* **Bermel, P., et al.** 25, s.l. : Optics Express, 2007, Vol. 15.

3. *Potential of amorphous silicon for solar cells.* **Rech, R. and Wagner, H.** 2, s.l. : Applied Physics A - Materials Science & Processing, 1999, Vol. 69.

4. *Determination of the thickness and optical constants of amorphous silicon.* **Swanepoel, R.** s.l. : Journal of Physics E: Scientific Instruments, 1983, Vol. 16.

5. *Optical gain in silicon nanocrystals.* **Pavesi, L., et al.** 11, s.l. : Nature, 2000, Vol. 408.

6. *Statistical ray optics.* **Yablonovitch, Eli.** 7, s.l. : Journal of the Optical Society of America, 1982, Vol. 72.

7. **Nelson, J.** *The Physics of Solar Cells.* London : Imperial College Press, 2003. 1860943497.

8. **Ji, Jing, Evans, Rhett and Basore, Paul.** *Glass Beads Coating Process. 487,580* United States of America, 2004.

9. *Texture etched ZnO:Al coated glass substrates for silicon based thin film solar cells.* **Kluth, O., et al.** s.l. : Thin Solid Films, 1999, Vol. 351.

10. *Development of highly efficient thin film silicon solar cells on tecture-etched zinc oxide-coated glass substrates.* **Muller, J., et al.** 1-4, s.l. : Solar Energy Materials and Solar Cells, 2001, Vol. 66.

11. Welcome to Pacific Solar. *Pacific Solar.* [Online] Pacific Solar, 2008. [Cited: May 9, 2009.] http://www.pacsolar.com.au/csg.html.

12. **Ji, Jing and Shi, Zhengrong.** *Texturing of Glass by SiO2 Film. 6,420,647* United States of America, July 16, 2002.

13. *Ordering and optical properties of monolayers and multilayers of silica spheres deposited by the Langmuir-Blodgett method.* **Szekeres, M., et al.** 11, s.l. : Journal of Materials Chemistry, 2002, Vol. 12.

14. *Nanosphere lithography: A materials general fabrication process for periodic particle array surfaces.* **Hulteen, J. C. and Duyne, R. P. Van.** 3, s.l. : Journal of Vacuum Science and Technology, 1994, Vol. 13.

15. *Two-dimensional nonclose-packed colloidal crystals formed by spincoating.* **Jiang, p., et al.** s.l. : Applied Physics Letters, 2006, Vol. 89.

16. *AngstromSphere silica sphere product datasheet.* [Online] 2005. [Cited: 3 22, 2009.]www.focenter.com/Fiber%20Optic%20Center/AngstromSphere/Data%20Sheets/PDFs/Dispersion%20Technique.pdf.

17. **Rancourt, James.** *Optical Thin Films.* s.l. : SPIE Press, 1987.

18. **Beckman, Michael.** *The effects of low pressure helium ion bombardment on hydrogenated amorphous silicon.* s.l. : Iowa State University, 2008.

19. *Amorphous-Silicon Solar Cells.* **Carlson, David E.** 12, s.l. : IEEE Transactions on Electron Devices, 1989, Vol. 36.

20. **Born, M. and Wolf, E.** *Principles of optics.* New York City : Cambridge University Press, 1980. 978-0521642224.

21. *Solar Simulation - Problems and Solutions.* **Emery, K., Myers, D. and Rummel, S.** s.l. : IEEE Photovoltaic Specialists Conference, 1988, Vol. 2.

22. **Reusswig, Philip.** *Measurement of minority carrier lifetimes in nanocrystalline silicon devices using reverse-recovery transient method.* s.l. : Iowa State University, 2008.

23. *Simple Method for the Preparation of Colloidal Particle Monolayers at the Water/Alkane Interface.* **Goldenberg, L. M., et al.** 14, s.l. : Langmuir, 2002, Vol. 18.

# ACKNOWLEDGEMENTS

I take this opportunity to thank the many people who helped and guided me in conducting this research. Thank you to Vikram Dalal for being my graduate advisor and financially supporting my research and degree. Thank you Atul Madhavan, Keqin Han, and Nayan Chakravarty for building solar cells on my substrates; I do not know how I can express my appreciation for the long hours you committed. I would also like to thank Max Noack for patience when giving me training, for guidance on my research, and for his handiwork that somehow keeps the MRC going each day. Thank you to Ben Curtin and Jason Jirak for sharing an office with me, laughing with me when things were going well and tolerating me when things were not going quite so well. I would also like to thank Ruth Shinar for letting me use her lab and for sharing advice throughout the project. Thank you to Dr. Kristen Constant and Dr. Rana Biswas for serving on my committee. Finally, thank you to all the students and researchers at the MRC for all the help, especially for helping to shorten the long hours with their friendship.